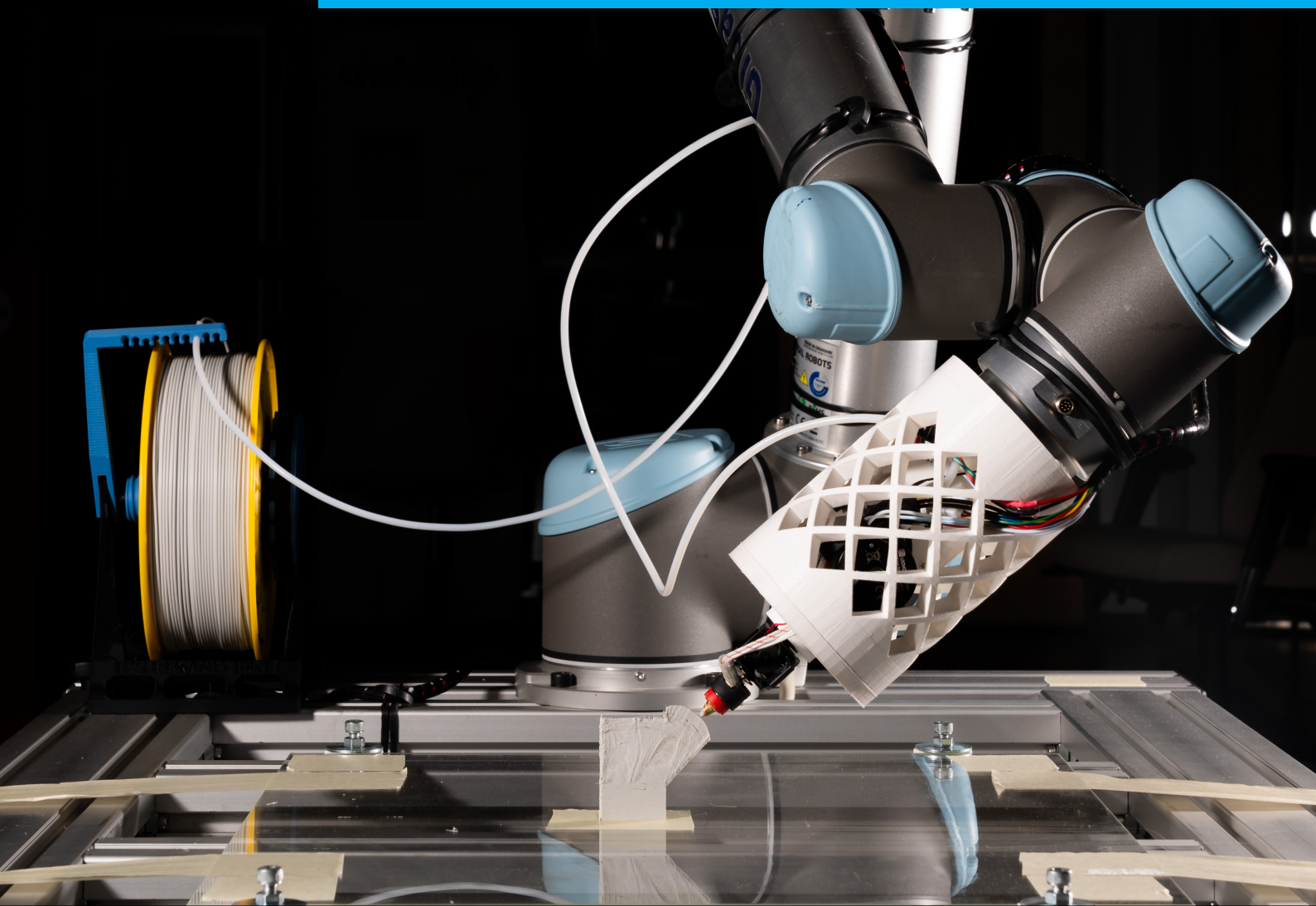Department of Precision and Microsystems Engineering

Limits of Curved-Layer Deposition in Robotic Additive Manufacturing

Tim Casper Geukers

TU Delft
Delft
University of
Technology

Challenge the future

Limits of Curved-Layer Deposition in Robotic Additive Manufacturing

by

Tim Casper Geukers

to obtain the degree of Master of Science

at the Delft University of Technology,

to be defended publicly on Friday June 27, 2025 at 2:30 PM.

TUDelft

Preface

Writing this preface feels surreal. After nine extraordinary and unforgettable years, my time as a student is drawing to a close. It is both strange and emotional to mark the end of this chapter with these words. This study period, and this thesis, would not have been possible without the support, guidance, and inspiration of many people, to whom I am deeply grateful.

First, I would like to express my sincere thanks to my supervisors, Can and Jun, for their invaluable guidance in shaping the scientific direction of this thesis. I am especially grateful to my daily supervisor, Manav, for his out-of-the-box thinking, thoughtful advice, and supportive check-ins throughout the process. I also owe much to Kai and Vibhas, whose models have been the inspiration, foundation and conclusion of this thesis.

I am fortunate to have had friends who stood by me during this journey. Many of them patiently endured me talking about this setup many, many, *many* times, and I am truly grateful for that. I would like to thank Stan in particular for his help with hardware selection and the creation of the setup, and Jasper for always being willing to help me solve problems, even from afar. As a friend group, we have experienced many things together, and I look forward to sharing many more of these *Labiel* and memorable moments with you all.

On a broader level, I want to thank my parents and my brother. They have supported me throughout these nine years of study, encouraging me even when I occasionally chose unexpected paths. I am also thankful to *de Boerderie*, my home for seven years, who provided me with a solid base whilst travelling through life. Finally, to Emma, my girlfriend, who has been a constant source of support during these final years. She always helped me put things in perspective, enabling me to think clearly when problems seemed overwhelming. I am deeply grateful for her patience, understanding, and encouragement.

To you, the reader: I hope you have enjoyed this small glimpse, window, or *Venster*, into my life. And I sincerely hope you enjoy this thesis. No pressure; it only is my magnum opus.

Tim Casper Geukers
Delft, June 2025

Abstract

Recent advances in multi-axial robotic additive manufacturing have enabled non-planar material deposition, introducing a new design freedom: the shape and sequence of individual layers during fabrication. This has led to the development of Space-Time Topology Optimisation (STTO), a method that simultaneously optimises both geometry and deposition sequence to reduce residual stresses and distortions, particularly in Wire-Arc Additive Manufacturing (WAAM). However, the fundamental manufacturing constraints that govern curved-layer deposition remain poorly defined. This thesis investigates and helps define the feasible domain of process and geometric conditions for curved-layer deposition through experimental studies using a robot-assisted additive manufacturing system.

A comprehensive literature review revealed a lack of explicit geometric criteria for printable curved layers, motivating the development of an empirical framework. To explore these constraints, a custom multi-axial robotic printing setup and a two-dimensional toolpath generator were developed, enabling controlled experiments into the geometric limits of non-planar deposition. Results from these experiments show that non-planar deposition is highly sensitive to temporal gradients in material flow rate. Abrupt changes in flow rate disrupt the dynamics of the material extrusion process and lead to defects in the printed parts.

Full-scale tests on optimised models further validated these findings. Despite the identified limitations, the models demonstrated promising manufacturability, as their gradual curvature resulted in relatively consistent flow rates. These results support the practical feasibility of STTO within WAAM and suggest promising directions for future research. Overall, this work advances the understanding of manufacturing limits in non-planar robotic additive manufacturing and helps bridge the gap between computational design and real-world production.

Contents

Nomenclature

Abbreviations

Abbreviation	Definition
ACT	Augmented Contour Tree
AM	Additive Manufacturing
Cobot	Collaborative robot
CNC	Computer Numerical Control
CAD	Computer-Aided Design
DED	Directed Energy Deposition
DOF	Degree of Freedom
G-code	Geometric Code
ME	Material Extrusion
PLA	Polylactic Acid
ROS	Robot Operating System
SF	Support Free
SQ	Surface Quality
SR	Strength Reinforcement
STTO	Space-Time Topology Optimisation
TO	Topology Optimisation
UR5	Universal Robot 5
WAAM	Wire-Arc Additive Manufacturing
WA-DED	Wire-Arc Directed Energy Deposition

<div align="right">

1

</div>

<div align="right">

Introduction

</div>

Additive Manufacturing (AM) describes several manufacturing processes that construct a 3D model by adding material in succession. The most well known AM method is Material Extrusion (ME), which is often used in traditional commercial 3D printers [1]. Over the past three decades, AM has transitioned from a niche innovation to a widely adopted manufacturing approach [2]. One promising AM technique is Wire-Arc Directed Energy Deposition (WA-DED), more commonly referred to as Wire-Arc Additive Manufacturing (WAAM), which enables large scale construction of a 3D model from metal [3]. However, WAAM faces various challenges that can impact its reliability and performance [4]. These challenges are described in more detail in section 1.1.

One potential approach to overcoming them is Space-Time Topology Optimisation (STTO), which extends traditional topology optimisation by incorporating the temporal aspect of material deposition. Through including this temporal aspect as a free design variable in the deposition sequence, STTO offers new possibilities for optimising structures for WAAM [5]. However, the freedom introduced by STTO must still respect manufacturing constraints to ensure that the optimised designs are feasible to produce. The integration of such constraints into STTO models remains an open question, and this thesis contributes by investigating which constraints may be necessary for practical implementation.

1.1. Background

WAAM is a metal AM process that combines an electric arc as a heat source with a metal wire as feedstock to deposit material layer by layer. This process is particularly advantageous for producing large-scale metal components, as it offers high deposition rates, material efficiency, and cost-effectiveness compared to traditional manufacturing methods. WAAM can work with various metals, including titanium, aluminium, and steel, making it suitable for applications in aerospace, automotive, and construction industries. Typically, a robotic arm is employed to control the deposition process, ensuring precise placement of material [6].

Figure 1.1: Deformation after unclamping an object manufactured with WAAM [7].

Despite its advantages, WAAM faces several challenges, with one of the most significant being residual stress and distortion. Due to the high thermal gradients introduced during the deposition process, residual stresses accumulate within the printed structure, leading to significant distortions once the component is unclamped from the build platform. These distortions can severely impact the dimensional accuracy, as can be seen in Figure 1.1, and mechanical performance of the final part [4]. Traditional solutions to mitigate these distortions include preheating the substrate, optimising the deposition path, and implementing post-processing techniques such as stress relief heat treatment [8]. However, these solutions add complexity, cost, and processing time to the manufacturing workflow .

Several research efforts have been dedicated to minimising residual stress and distortion in WAAM. One approach involves path planning optimisation, where deposition sequences are strategically designed to distribute heat more evenly and reduce thermal gradients [9]. A promising solution involves the integration of topology optimisation (TO) with AM.

Traditional TO is a computational design approach that optimises the distribution of material within a domain based on specific constraints and objectives. By minimising a predefined cost function, such as weight, compliance, self-support or stress, TO generates the geometric layout that is optimised for performance while reducing material usage [10]. An example of such an optimised design can be seen in Figure 1.2.

(a) 3D-printed industrial frame with several overhangs requiring support structures.

(b) 3D-printed industrial frame after optimisation, redesigned for support-free printing.
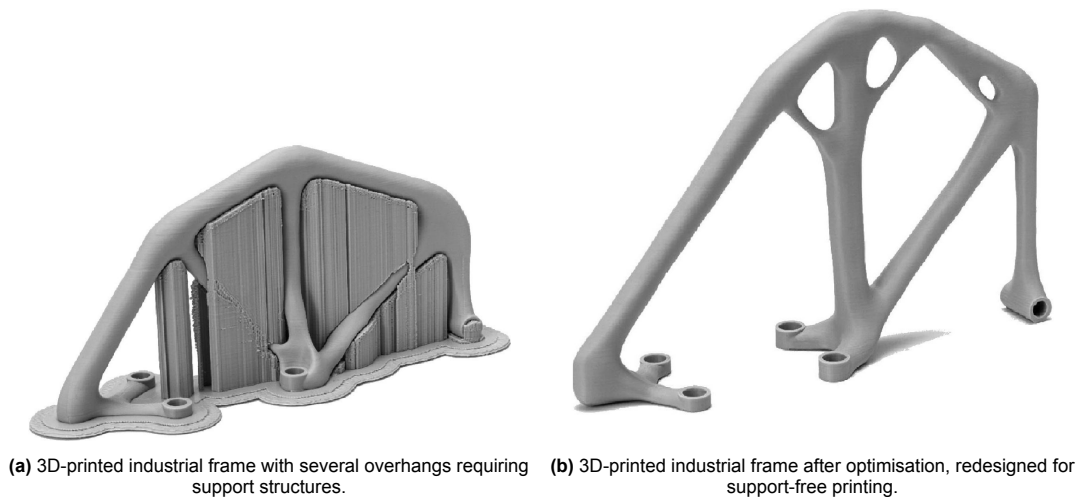
Figure 1.2: A 3D-printed industrial frame before and after optimisation. The objective of the optimisation was to achieve a self-supporting design suitable for additive manufacturing [11].

TO is unaware of the temporal nature of AM, which is generally not a concern for traditional commercial 3D printers which are constrained to 2.5D to avoid collision with the object. As a consequence TO focuses solely on optimising the final structure, without considering the sequence of material deposition.

However, recent advance in multi-axial robotic additive manufacturing have enabled non-planar deposition, where layers can follow curved paths rather than being flat. With these curved paths one can create improved mechanical properties in certain directions, reduce support and have a better surface quality. More importantly, it introduces a free design variable: the layer shape and sequence [12].

With the additional flexibility, manufacturing is no longer a passive step after TO, it becomes an integral part of the part optimisation process. This shift motivated Space-Time Topology Optimisation (STTO), which simultaneously optimises both the geometrical layout and its fabrication sequence.

Unlike traditional TO, which focuses solely on the topology, STTO accounts for the evolution of the structure during material deposition, enabling optimisation of the fabrication sequence and layer orientation [13]. This approach provides an opportunity to proactively mitigate residual stresses and distortions by adjusting the order and direction in which layers are built [14].

STTO has the potential to revolutionize WAAM by generating optimised deposition strategies that minimise thermal residual stresses while maintaining structural integrity. By incorporating mechanical sim-

ulations, STTO can predict and minimise distortions during the design phase, ensuring that the final printed part remains within acceptable tolerances. An example of this can be seen in Figure 1.3. It can be seen that the simulated deformation with optimised layers based on the STTO model has significantly reduced the theoretical distortion of the part.
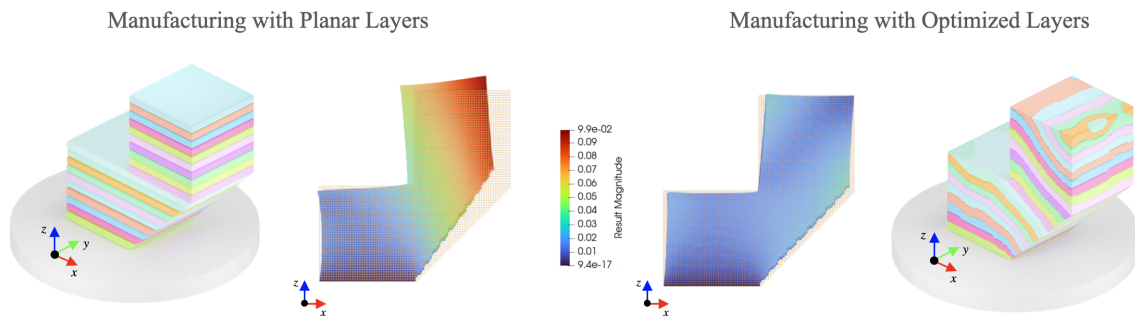
Manufacturing with Planar Layers   Manufacturing with Optimized Layers

Figure 1.3: Simulated deformation difference between planar- or optimised layers by STTO for WAAM [15].

However, despite its promising advantages, STTO faces significant challenges in practical implementation, particularly concerning manufacturability. One of the key features of STTO is its reliance on non-planar layers, which require multi-axial fabrication setups for execution. Unfortunately, the layers generated by STTO often result in complex, highly curved deposition paths that may not be feasible to print. These paths can introduce severe overhangs, excessive tool tilting, or inaccessible regions that violate the physical limitations of robotic WAAM systems [14]. While multi-axial WAAM setups, ranging from 4 to 7 degrees of freedom, have been constructed, they cannot accommodate all possible deposition paths due to constraints such as collision avoidance, tool reachability, and build stability [12]. These limits for multi-axial deposition for non-planar models are not yet fully defined, which is why current STTO models can not be verified for manufacturability without actually printing them.

1.2. Research Objective

The aim of this thesis stems from the current inability to reliably verify the manufacturability of non-planar models in additive manufacturing. The central research question guiding this thesis is:

What are the fundamental manufacturing constraints that define the feasible domain for curved-layer deposition using a robot-assisted additive manufacturing system?

This question will be addressed in the upcoming chapters. A literature review is conducted in chapter 2 to identify existing constraints in non-planar slicing. While these constraints ensure manufacturability and serve specific design objectives, they do not explicitly define the geometric limits. Such limits are necessary to validate the manufacturability of each layer. Based on these insights, the development of the multi-axial printing setup is detailed in chapter 3. Finally, chapter 4 presents and discusses the experimental findings used to establish the fundamental manufacturing constraints. Based on these results the thesis is concluded in chapter 5. Recommendations made for further research can be found in chapter 6.

<div align="right">

2

</div>

Overview of non-planar slicing

This chapter provides an overview of recent research in non-planar additive manufacturing, with a particular focus on non-planar slicing strategies. In conventional 3D printing workflows, a digital model of the target object is first created, which is then converted into a set of planar layers using a slicing software. These layers guide the deposition process during fabrication. While traditional slicing assumes flat, horizontal layers, advances in computational design and multi-axis printing systems have enabled the generation of curved, or non-planar layers.

The software responsible for generating these layers is known as a slicer. Unlike standard planar slicers, non-planar slicers must consider additional geometric and mechanical constraints to ensure manufacturability.

This chapter first reviews various methods for generating non-planar layers and identifies the associated manufacturing constraints, as detailed in section 2.1, 2.2, and 2.3. In section 2.4 the second critical function of a slicer is explored: determining the fabrication sequence. In section 2.5 the current state of the art in non-planar slicing is discussed, which highlights the recent advancements and gaps in the literature. These advancement and gaps are then summarised in section 2.6 from which the main focus of this thesis originates.

2.1. Non-Planar Deposition on Pre-Shaped Surfaces

In 2019, Chen et al. [16] published an innovative study on the additive manufacturing of thin-shelled, curved models. Their work marked a significant milestone in the advancement of non-planar slicing by presenting both a theoretical framework for their method and a practical demonstration of its feasibility. To enable their non-planar printing approach, the authors developed not only a specialized slicing algorithm but also a hardware system capable of executing the fabrication.
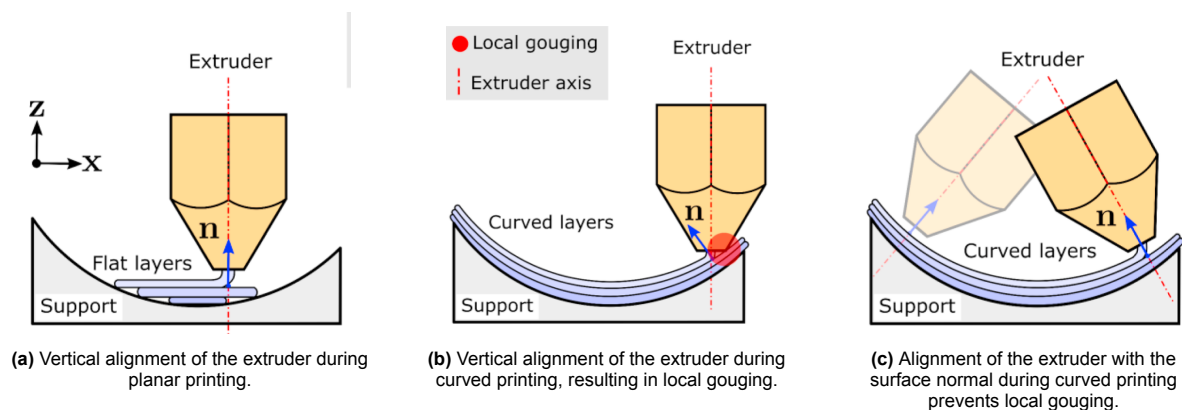

(a) Vertical alignment of the extruder during planar printing.

(b) Vertical alignment of the extruder during curved printing, resulting in local gouging.

(c) Alignment of the extruder with the surface normal during curved printing prevents local gouging.

Figure 2.1: Illustration of how extruder alignment affects the printed layers in planar and curved printing. Adapted from [16].

A critical design consideration in their hardware setup was determining the orientation of the extrusion axis during deposition. As illustrated in Figure 2.1b, maintaining a fixed nozzle orientation, as is common in traditional planar printing, can lead to local gouging when printing on curved surfaces. To address this issue, Chen et al. [16] employed a five-axis robotic system, ensuring that the nozzle remains aligned with the local surface normal at each point of material deposition. This alignment minimises the risk of surface interference and maintains consistent material flow.

Focusing specifically on the fabrication of thin-shelled structures, the authors proposed printing onto a pre-curved substrate used as a support, typically made of foam or another easily shaped material. To accommodate the complex geometry of the target shapes, a variable-depth slicing algorithm was introduced. This algorithm allows for continuous variation of layer height according to the local curvature, enabling the printer to emphasize geometric features by increasing layer thickness at convex regions and reducing it at concave regions.

By integrating the variable-depth slicing method with a custom path planning algorithm, the researchers successfully developed a functional non-planar slicing workflow for thin-walled geometries. The resulting prints, produced using a five-axis robotic arm, are shown in Figure 2.2.
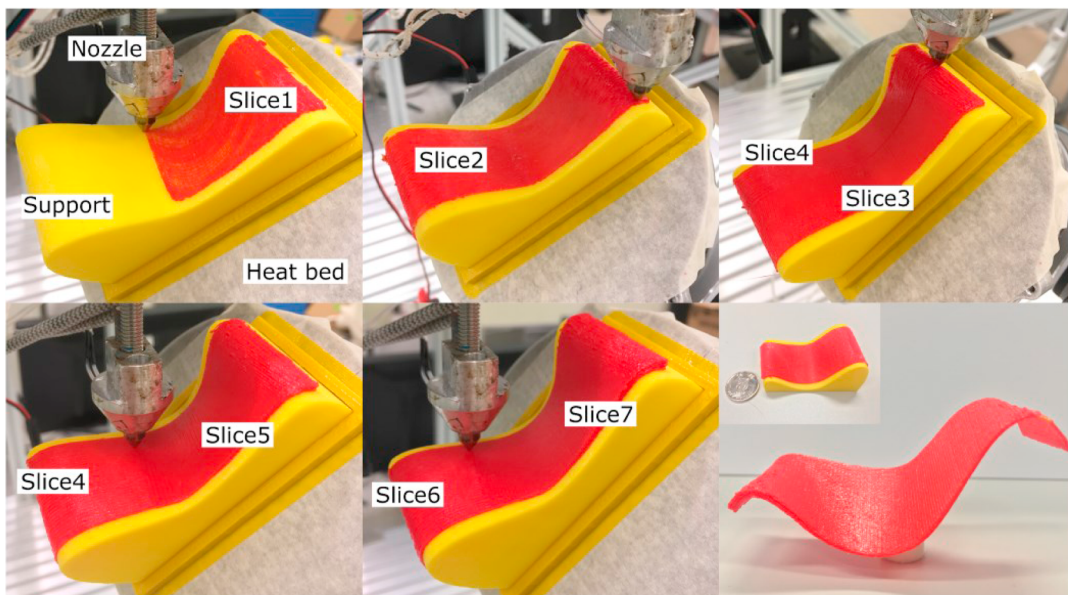

Figure 2.2: Demonstration of printing a thin-shelled model on a five-axis robotic printing setup [16].

2.2. Curved Geometry through Gradual Elongated Layers

While Chen et al. [16] successfully demonstrated the printing of curved surfaces, the curvature in their work was not generated during the printing process itself. Instead, the prints were deposited onto a pre-shaped, curved support structure. In most additive manufacturing processes, where printing typically occurs on a flat build surface, it becomes essential to generate curvature during fabrication.

To address this challenge, Li et al. [17] proposed a vector field-based curved slicing method, which enables the formation of curved geometries by gradually elongating the stacked layers. This cumulative elongation results in a progressive curvature throughout the print, as illustrated in Figure 2.3a. By initiating the stacking process from the lower right corner and incrementally increasing the layer height, a curved profile is achieved.

This method demonstrates improved mechanical properties compared to conventional planar-layer printing. This improvement stems from the interlocking between curved layers, which promotes stronger bonding and more uniform stress distribution compared to the conventional stacking of planar layers. However, the presented method faces challenges in achieving consistent part quality. As can be observed in Figure 2.3b, small gaps appear between deposited layers. These defects are attributed to a staircase effect that emerges internally during the layer-stacking process. While the curved layer
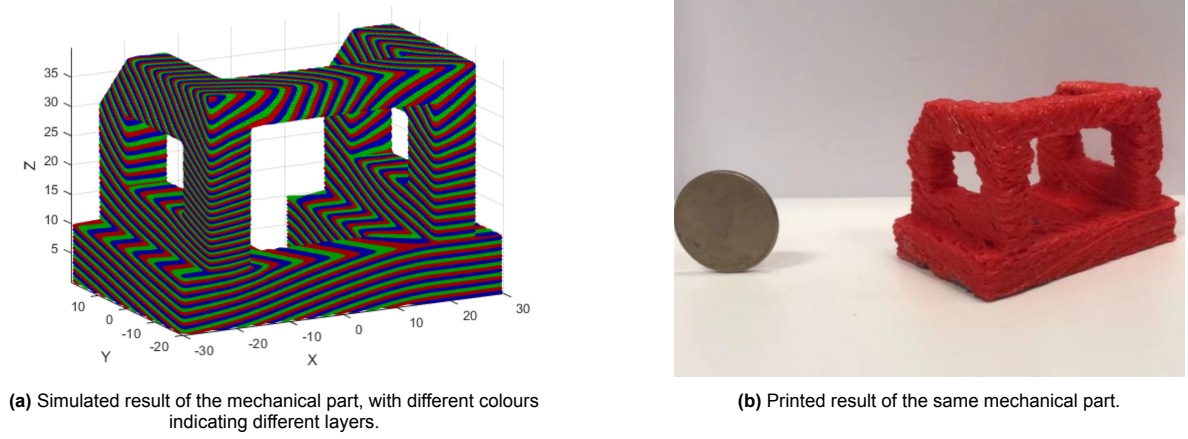
(a) Simulated result of the mechanical part, with different colours indicating different layers.

(b) Printed result of the same mechanical part.

Figure 2.3: Simulated (left) and printed (right) results of the mechanical part. Adapted from [17].

above may partially seal these gaps, it often fails to completely fill them. Additionally, minor misalignments between successive layers can result in surface irregularities, ultimately affecting the accuracy and adhesion of subsequent layers.

2.3. Curved Geometry through Variable Layer Thickness

As demonstrated in section 2.2, the use of uniformly thin sub-layers often results in the formation of gaps within the printed structure. To address this issue, an alternative approach was explored, one that had previously been applied by Chen et al. [16] in the context of thin-walled structures, though without extending it to the printing of fully volumetric objects on a flat build surface.

The concept of using varying layer thickness was formally introduced by Etienne et al. [18] in the development of CurviSlicer. Their method enabled the generation of curved layers on conventional 2.5-axis consumer-grade printers, significantly expanding the accessibility of non-planar printing. This approach was later adapted by Lau et al. [19] for use in multi-axis printing systems, where it demonstrated further potential. A schematic representation of this method is shown in Figure 2.4a.

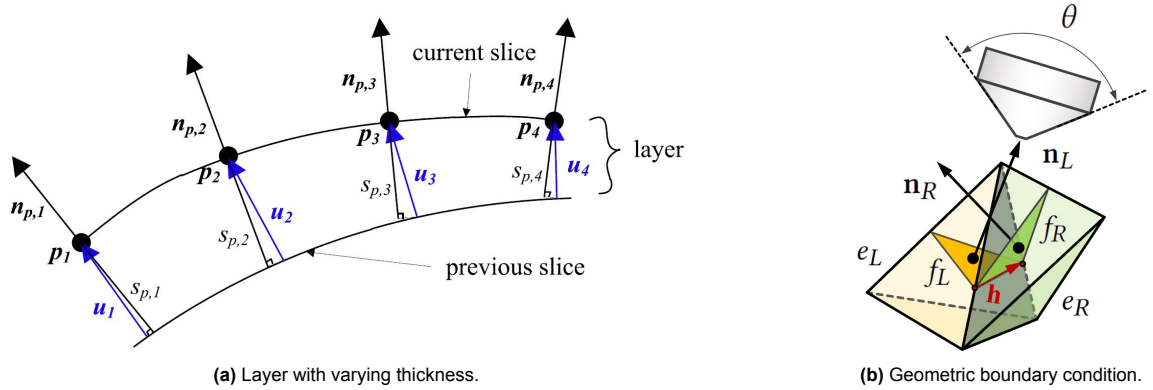**(a)** Layer with varying thickness.

(b) Geometric boundary condition.

Figure 2.4: Schematic illustrations relevant to curved printing. (a) A layer with varying thickness, where n_p denotes the print direction at point p and s_p defines the local layer thickness [19]. (b) A geometric boundary condition that enforces a minimum nozzle clearance angle θ. The angle between adjacent faces f is determined from their normals n [20].

By gradually varying the thickness of each deposited layer, the slicer can incrementally increase the global gradient of the printed object, allowing for the formation of continuous curved surfaces. However, this method has limitations. Since a significant gradient requires the accumulation of multiple layers, it cannot be used effectively near the build plate. Moreover, the maximum achievable layer thickness is constrained by the nozzle diameter. Typical printable layer heights range between 25% and 75% of the nozzle diameter [21].

Compared to Chen et al.'s [16] method, which relied on thin sub-layers and pre-curved substrates, the varying layer thickness approach offers a clear advantage: the absence of internal air gaps, as shown in Figure 2.5. This leads to more consistent material deposition and improved surface quality.
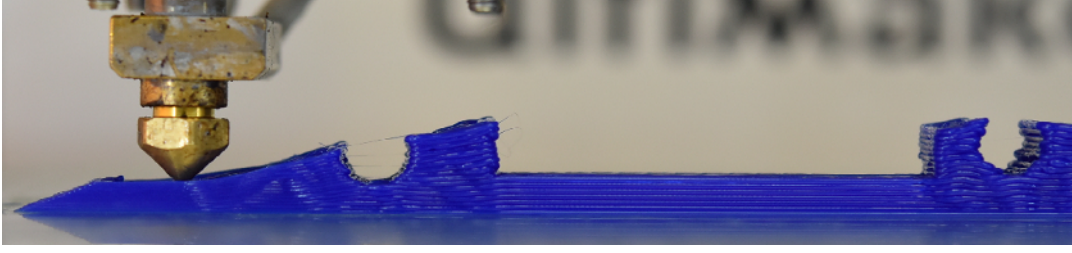
Figure 2.5: Mid-print example of a curved layer generated using CurviSlicer [18].

Nevertheless, the method imposes additional geometric constraints to avoid collisions between the nozzle and the part. Specifically, the slicer must ensure that adjacent surface faces do not form an angle smaller than the nozzle's minimum clearance angle, θ. As shown in Figure 2.4b, the normals n_L and n_R of adjacent faces f_L and f_R must not form an angle less than θ, thereby ensuring sufficient clearance for nozzle movement. When surface features become densely packed, there is also a risk of gouging if the nozzle remains aligned with the surface normal. This risk can be mitigated by incorporating collision awareness into the fabrication sequence, which will be discussed further in section 2.4.

2.4. Fabrication Sequence

As mentioned before, slicing the object into several layers is not the only function of slicing software. It also needs to determine the correct fabrication sequence to ensure that every layer is actually reachable at the moment it needs to be printed, and if this is not the case, ensure that the layers are redistributed in a manner that it is possible to create a fabrication sequence which makes accessible and printable layers.

A very powerful method to ensure printability has been shown by Lau et al. [19]. This method divides the object into several segments by using an Augmented Contour Tree (ACT), which splits the model on every intersection point. These components then again split into several slabs. With all these slabs in place, the model now tries to remove each slabs from top to bottom. Whenever it encounters multiple slabs to be removed it continues to calculate the possibilities, and if the removal of these slabs creates a situation where no slabs can be removed it discards this possibility. This method of removal can than be reversed to create the order of construction. The full flow-chart of this process can be found in Figure 2.7.

It most be noted that this implementation only works if the final shape of the object is known. It can therefore not be fully transferred to all aspects of the STTO model, since it does not allow for concurrent optimisation of the stucture and sequence. Dai et al. [22] managed to find another way to specify the layer setup and create a working fabrication sequence. In their research they found that it is possible to find a working fabrication sequence, without knowing what the final shape of the object will be. Instead
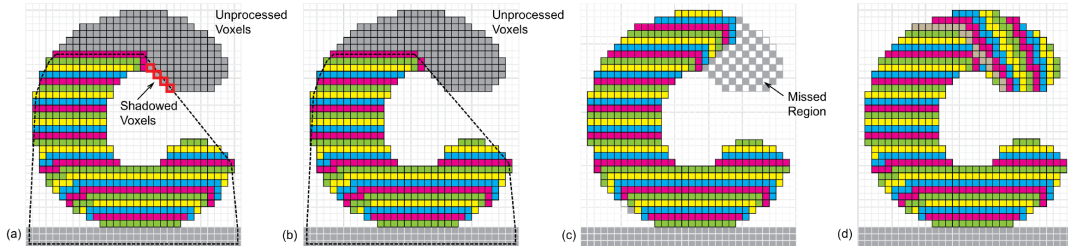
Figure 2.6: (a) A critical step where shadowed voxels appear (b) Optimised result with shadowed voxels (c) The result without optimisation, a large part is missing (d) The result with the optimisation, the full design space can be printed [22].
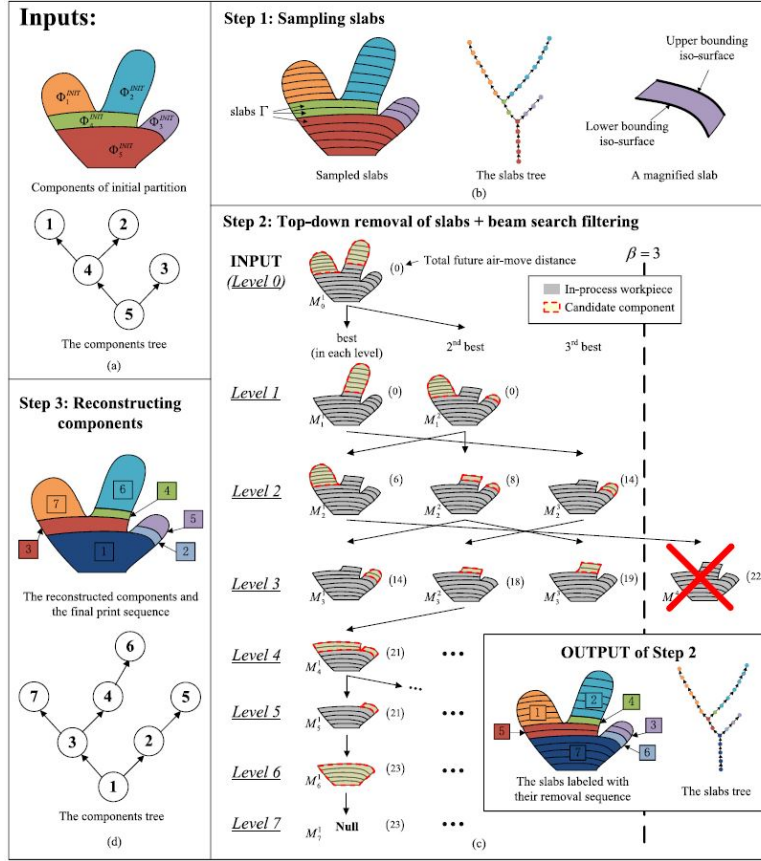
Figure 2.7: (a) The initial partition using ACT. (b) Splitting the components into several slabs. (c) Top-down removal of slabs. (d) Reversing removal sequence to create a feasible fabrication sequence [19].

of optimising the order of several segments, like Lau et al. [19] did, their implementation optimised for that every new layer should keep as much of the free design space still reachable. This can be seen in Figure 2.6. Their method involves discretizing the different layers into voxels. Once a layer is finished they calculate how much of the free design space is still reachable, and if it is not 100% reachable they show which voxels are unreachable for the next layer and "shadow" them. As a result a large part of the design space can never be printed, and thus a large part of the design space is left empty. With the help of the model of Dai et al. [22], it is possible to find a layer that leaves the full design space reachable, resulting in a fully used design space and therefore fully printed object.

It is this model, and definition, that can be transferred to STTO. Every layer should try to leave as much of the design space still reachable, ensuring that the STTO model can still freely optimise in the resulting design space.

2.5. State-of-the-Art: S^3-Slicer

The current state-of-the-art in non-planar slicing is represented by the S^3-Slicer, developed by Zhang et al. [20]. This slicer builds upon previously introduced methods and geometric constraints to generate non-planar toolpaths tailored for multi-axis additive manufacturing systems. Crucially, it allows for user-defined preferences, enabling a high degree of customization in the slicing process.

The S^3-Slicer is capable of optimising for three primary objectives: support-free (SF) fabrication, enhanced surface quality (SQ), and strength reinforcement (SR). Users may select any combination of these objectives, after which the slicer computes a corresponding non-planar toolpath that satisfies the selected criteria. Representative outcomes of these optimisation modes are shown in Figure 2.8a, while a printed result is displayed in Figure 2.8b.

This work highlights the expansive design space offered by non-planar layer fabrication and demonstrates how the orientation, length, and thickness of layers can be strategically manipulated to serve different functional goals. Importantly, it also suggests that the implementation of STTO models is becoming increasingly feasible, provided that relevant manufacturing constraints are properly accounted for.
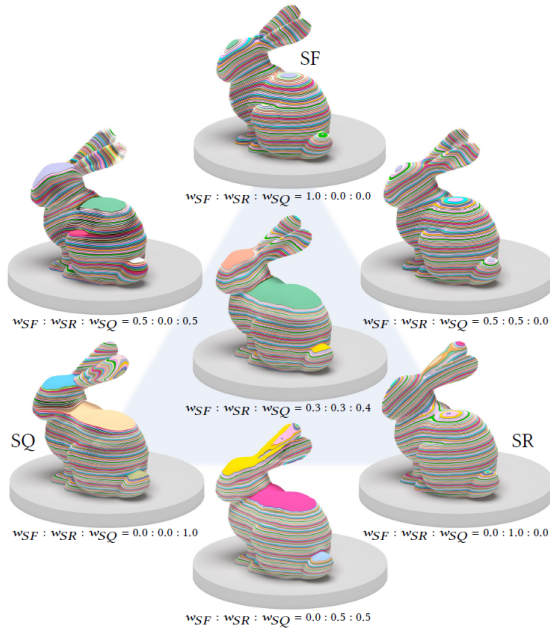
(a) Optimised geometries produced using different S^3-Slicer objectives [20].

(b) Printed result of one of the S^3-Slicer toolpaths [20].

However, even though this slicer shows tremendous possibilities, it does not utilise the full geometrical potential of non-planar deposition. Due to this no conclusions can be drawn regarding the geometrical limits of multi-axial deposition for non-planar layers.

2.6. Summary of Manufacturing Constraints and Research Gaps

Based on the research reviewed in this chapter, several key manufacturing constraints for non-planar printing can be identified:

- The thickness of each deposited layer must remain within a permissible range, typically constrained by the nozzle diameter.
- The minimum angle between adjacent surface facets must not fall below the nozzle's clearance angle, as illustrated in Figure 2.4b, to prevent tool collisions.
- The overhang angle at any point must remain below the maximum printable threshold to ensure structural support during deposition.
- Each layer must be printed either on a previously deposited layer or directly on the build platform; unsupported printing is not feasible.
- Each subsequent layer should minimise regions of the model that become inaccessible to the print head during fabrication.

These constraints are primarily aimed at avoiding collisions between the printhead and the printed geometry during fabrication. Notably, aside from the constraint on layer thickness, there is currently no geometric limitation defined for the allowable slope of a surface or within a layer.

Identifying these additional geometric constraints is critical for advancing the verifiability of non-planar designs without relying on physical prototyping. The findings presented in chapter 4 will build on this foundation by providing empirical insights into the geometric feasibility of non-planar printing approaches.

3

Multi-axial printing setup

This chapter outlines the design and configuration of the multi-axial printing setup developed for this thesis. The hardware components are detailed in section 3.1, along with a discussion of how each element was selected based on the manufacturing constraints presented earlier. Control mechanisms for the hardware and the software implementation required to operate the system are covered in section 3.2. This section also discusses the software tools used to generate instructions for converting digital models into movement and extrusion commands.

3.1. Hardware

Conventional consumer-grade 3D printers typically operate based on planar layer deposition and feature translational movement along all three Cartesian axes. However, during active printing, motion along the z-axis is generally restricted to a single direction to prevent collisions between the printhead and the model. By relaxing this restriction, it becomes possible to print non-planar layers to a limited extent, as demonstrated by Etienne et al. [18]. To fully exploit non-planar printing capabilities, a multi-degree-of-freedom (DOF) setup is required, incorporating additional rotational DOFs. These rotational DOFs can be added either to the printhead or the print platform, depending on the intended geometries and performance goals.

Four-axis 3D printing setup The addition of a single rotational DOF can be achieved either by rotating the nozzle about the x- or y-axis or by rotating the print platform around the z-axis. Such four-axis setups are relatively uncommon due to their limited enhancement in printable geometry range [23].

Five-axis 3D printing setup A more versatile configuration involves the addition of two rotational DOFs. Hong et al. [24] proposed a reliable method for upgrading a traditional three-axis printer by incorporating a two-axis rotational mechanism beneath the printing platform, allowing rotation around both the y-axis and the local z-axis. Alternatively, the rotational DOFs can be integrated into the printhead itself, typically by enabling rotation about the z-axis in combination with either the local x- or y-axis. A hybrid approach can also be used, where one rotational axis is added to the printhead and another to the build platform.

Six-axis or more 3D printing setup A six-DOF printing system generally employs a six-axis robotic arm as the primary actuator [23]. In such setups, either the printhead or the platform can be mounted to the robotic arm, while the other remains stationary. Additional DOFs can be integrated beyond six, for instance, by mounting the platform on a rotating base while also using a six-axis robotic arm to manipulate the printhead. These enhancements increase the system's flexibility and printable range while minimising inaccessible regions.

The multi-axial setup developed for this thesis features six DOFs, realized entirely through the motion capabilities of a robotic arm that manipulates the printhead. The print platform remains in a fixed po-

sition beside the arm. This architecture aligns with common WAAM systems, enhancing the industrial relevance of the toolpath validation process [25]. Additionally, the selected hardware allows for further expansion, as unused stepper driver outputs remain available on the chosen control board. The following subsections detail the three primary hardware components: the robotic arm, the printhead, and the printing platform.

3.1.1. Robotic arm

To achieve six degrees of freedom, the Universal Robot 5 (UR5) robotic arm is employed, as shown in Figure 3.1. The UR5 features a reach of 850 mm and a positional repeatability of ±0.1 mm [26]. It operates over an IP-based interface, allowing communication with other networked devices for command input and status reporting. This network-based interface is the primary method of controlling the robotic arm in this setup.

The UR5 is mounted on a sturdy worktable, and its end effector interface allows various tools to be attached using four screw holes. In this implementation, the custom-designed printhead is mounted at the tip. As a collaborative robot (cobot), the UR5 is designed to operate safely alongside human operators without physical barriers [27], improving accessibility and ease of use even during motion.
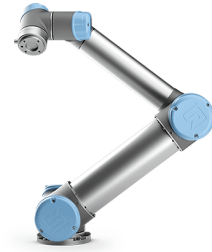
Figure 3.1: The Universal Robot 5 [26]

3.1.2. Printhead

The hot end of a ME printer typically consists of three main components: the heat break, the heat block, and the nozzle. These components and their arrangement are illustrated in Figure 3.2. The heat block is responsible for heating the system, while the heat break serves to dissipate heat, preventing it from propagating further up the filament path. The molten filament is deposited through the nozzle, whose precise diameter ensures accurate volumetric control during material extrusion. Filament is fed into the system from the top, with the feed rate governed by the extruder. By adjusting the extruder speed, the flow rate of the filament can be increased or decreased accordingly

The printhead is mounted at the end of the UR5 and comprises a combination of off-the-shelf components integrated into a custom designed attachment. The following components are used, and their placement is shown in Figure 3.3a and 3.3b.
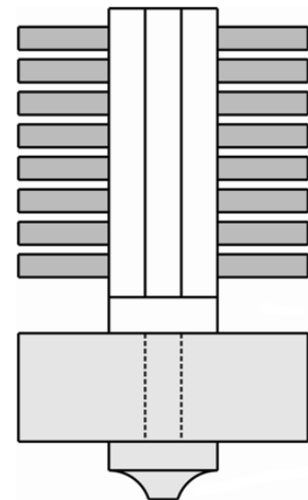
Duet 3 Main Board 6HC The printing system is controlled by a Duet 3 Main Board 6HC. Like the UR5, it is IP-based and can send and receive data over a shared network. The board offers sufficient processing power and available connections to support future system upgrades [28]. It is installed remotely from the printhead, with long electrical wires connecting the board to the printhead components.

Figure 3.2: Schematic illustration of a typical hot end used in FDM printing.

Orbiter v2.0 To ensure material extrusion, the Orbiter v2.0 extruder is used. Due to the distance between the filament spool and the printhead, a result of the UR5's range, a powerful extruder with reliable grip is required. Furthermore, due to the inherent nature of non-planar printing the flow rate differs greatly over each layer. An extruder with high acceleration is therefore an additional prerequisite. The Orbiter v2.0 satisfies these criteria and plays a crucial role in ensuring print reliability during non-planar operations [29].

E3D Revo Micro For heating, the compact E3D Revo Micro hotend is used [30]. Its small footprint is well-suited to the spatial constraints inherent in multi-axial printing. Furthermore, the system utilizes a belt nozzle designed for angled extrusion, supporting printing at inclinations up to 45° [31], thereby expanding the achievable geometries without risk of collision.

Part cooling fan   A part cooling fan is integrated into the design but was not connected during the presented experiments. Given the higher cooling requirements associated with WAAM, the fan was excluded to maintain better comparability with industrial conditions. Nevertheless, provisions for its installation have been made to enable future experimentation. An additional funnel will be necessary to direct the airflow from the base of the printhead to the extrusion point.

The printhead housing is a custom-manufactured 3D-printed assembly, consisting of three primary components: a baseplate, a component mounting piece, and an enclosure. These parts are connected using threaded inserts and screws. The baseplate includes a threaded section for precise central placement of the E3D Revo Micro. The enclosure has visual access holes as to inspect each component during motion. The rigid connection between the components and the UR5 ensures precise positioning of the nozzle tip based on the motion of the UR5. An assembled view of the printhead is shown in Figure 3.3c.

(a) Back view of the printhead without enclosure.

(b) Side view of the printhead without enclosure.

(c) Side view of the printhead.

Figure 3.3: Several renders of the custom designed printhead.

3.1.3. Printing platform

The printing platform is inspired by conventional consumer-grade 3D printers, employing a glass surface due to its inherent flatness. While typical printers use heated platforms ($\approx 60\ ^\circ$C) to promote adhesion, this setup substitutes thermal adhesion with increased surface roughness. By covering the glass with standard scotch tape, sufficient adhesion can be achieved without heating.

To ensure platform levelling, four adjustable spacers are installed, one at each corner. A wireframe diagram of a spacer is shown in Figure 3.4. Each spacer consists of a spring-loaded washer assembly that can be adjusted via a screw and nut mechanism, enabling millimetre-level positional control.

Because collision avoidance is critical, a virtual representation of the setup has been created, as shown in Figure 3.5a. This model includes the UR5
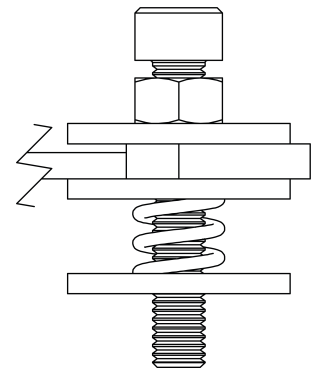

Figure 3.4: Wireframe of the printing platform spacer.

with the printhead, the worktable, the filament spool, and the printing platform with its spacers. Despite precise physical measurements, slight misalignments can occur during assembly. Thus, the UR5 is employed for calibration. A calibration routine drives the UR5 to expected corner positions, allowing the platform to be adjusted such that the nozzle tip just contacts the surface. This ensures that both levelness and spatial accuracy are aligned with the virtual model. Some additional modifications have been taken regarding the stiffness of the whole printing table. The modifications and their effect on the vibrations are shown in Appendix A.

(a) Virtual representation of the setup   **(b)** Actual multi-axial printing setup
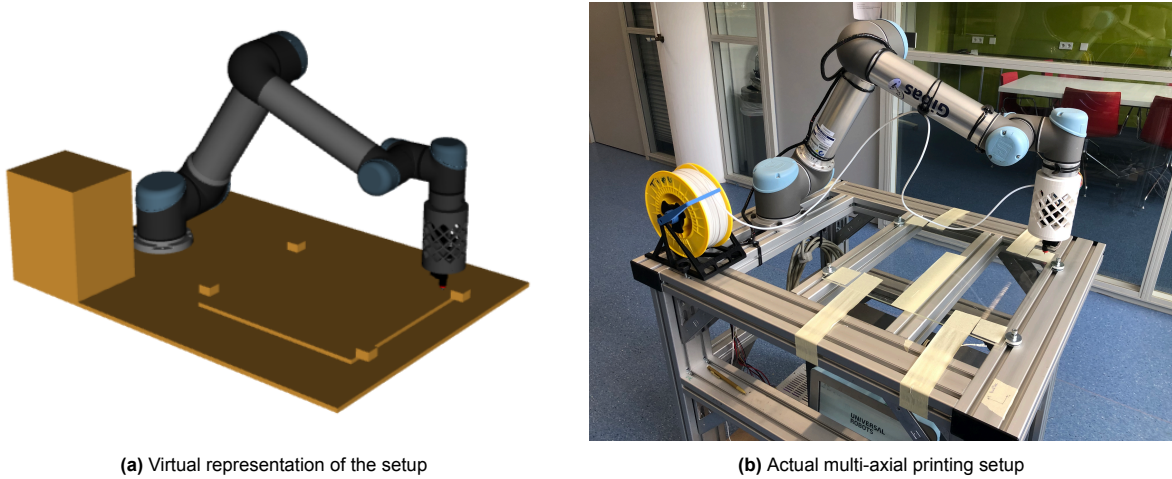
Figure 3.5: Side-by-side comparison of the virtual and physical multi-axial printing setup.

3.2. Software

This section presents the software required to operate the multi-axial printing setup. The entire printing process can be divided into two primary stages: pre-processing and processing. Both stages are executed within the ROS (Robot Operating System) environment and are elaborated in subsection 3.2.1. Additionally, the creation of the instruction file, commonly referred to as G-code, is described in subsection 3.2.2. This instruction file contains all motion and printing parameters for each path in the model. An overview of the full software architecture is shown in Figure 3.6 and is published online[1].
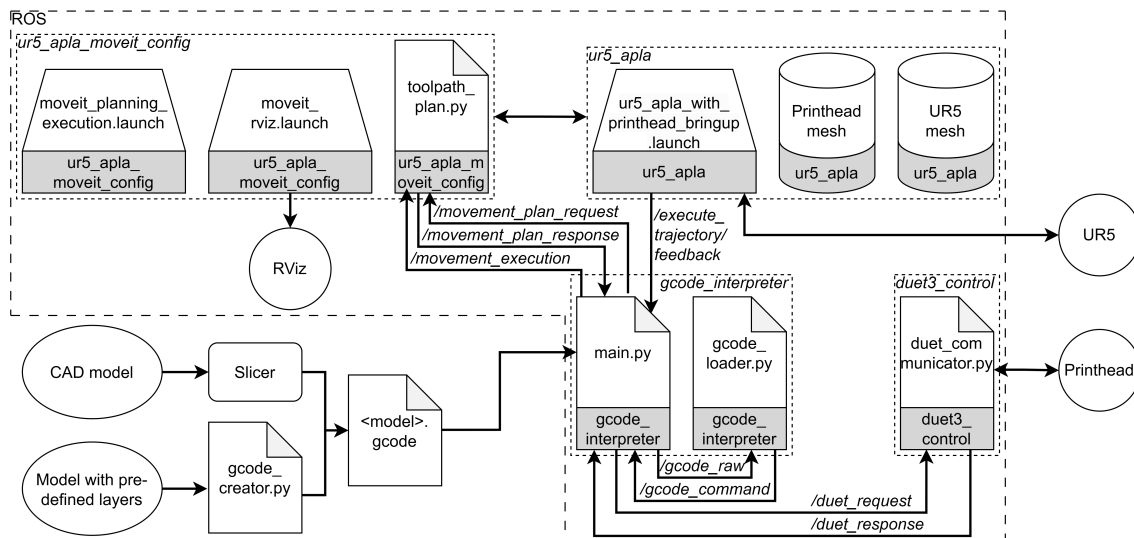

Figure 3.6: The full software architecture

---

[1] https://github.com/90zaza/ROS-UR5-APLA

3.2.1. ROS Topology

ROS is an open-source collection of software libraries and tools designed for robotics applications. Due to its open-source nature, it evolves rapidly and supports various versions [32]. ROS Noetic, running on Ubuntu 20.04, has been used for this setup. To meet real-time processing requirements a real-time kernel has been deployed in the build of Ubuntu 20.04. This ROS and Ubuntu version is recommended for the UR-series [33].

ROS organizes functionality into packages, nodes, and topics. A package is the primary organizational unit, containing code, configuration files, and data. Packages are outlined in dashed boxes in Figure 3.6. A node is a process that performs computation. Nodes are illustrated using file-like icons in the figure. The final important piece of the ROS infrastructure are topics, which functions like a radio frequency: nodes publish data to topics, and other nodes subscribe to receive that data. Arrows with italicized labels represent topics in Figure 3.6. Standardized message structures ensure that publishers and subscribers can interpret the transmitted information correctly.

All ROS elements are enclosed by a large dashed line in the architecture diagram. The system comprises five primary packages:

- `ur5_apla`: Contains all kinematic and visualization data for the UR5 and printhead, including drivers. Acts as the interface between the virtual and physical setups.
- `ur5_apla_moveit_config`: Hosts the motion planning framework and inverse kinematics solver, integrated with a visualisation tool called RViz.
- `duet3_control`: Provides the framework for communication with the Duet 3 Main Board 6HC.
- `gcode_interpreter`: Contains `main.py`, which is the orchestrator of the workflow. It manages communication and control across all other packages.
- `fdm_msgs`: Defines custom message formats used across topics. These messages are essential for structured communication but are not depicted in the architecture diagram.

The overall workflow in ROS is divided into two main subsystems: pre-processing and processing, which are described in the following subsections.

Pre-processing
The goal of the pre-processing step is to pre-calculate all essential variables for both the robotic arm and the printhead, such as flow rate and motor acceleration. Pre-computing these values ensures smooth, continuous operation, since delays in on-the-fly computation could interrupt motion. For instance, with instructions executing in as little as 0.06 seconds, real-time computation may not keep pace. Offloading this computational burden beforehand mitigates the risk of timing issues.
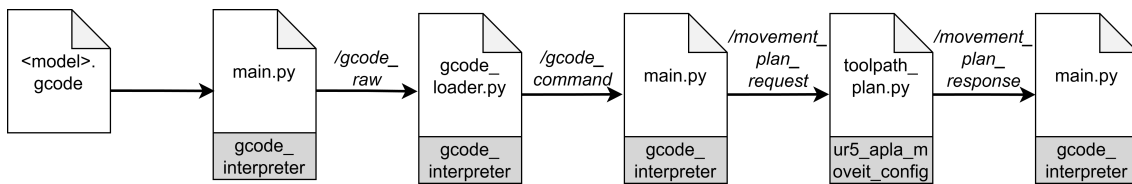

Figure 3.7: The pre-processing step, visualized as a sequential pipeline

The G-code file (`<model>.gcode`) is loaded by `main.py`, entering the ROS communication pipeline. The following steps summarize the subsequent process:

1. Each line of G-code is published to the topic *gcode_raw*, with a sequence ID to maintain execution order.

2. `gcode_loader.py` subscribes to *gcode_raw* and classifies each line as movement, printing, or combined commands. It extracts key parameters like position, orientation, speed, and filament length.

3. Parsed commands are republished in a new communication structure to *gcode_command*, including the same sequence ID.

4. `main.py` filters these messages. Movement commands are send to */movement_plan_request*, while pure printing commands are temporarily stored.

5. `toolpath_plan.py` computes inverse kinematics and required accelerations using tools from `ur5_apla_moveit_config`, then publishes executable robot commands.

6. `main.py` collects these commands on *ur5_apla_moveit_response*, associates them with their sequence IDs, and assembles the instructions in chronological order. Consecutive movement commands are concatenated, optimising for continuous motion.

At the end of the pre-processing step, `main.py` is left with a list filled with printing and movement commands which can be interpreted by the respective hardware system.

Printing process

During printing, synchronization between the UR5 and the printhead is critical. The architecture ensures synchronized execution by incorporating feedback mechanisms from the UR5. The process is visualized in Figure 3.8.
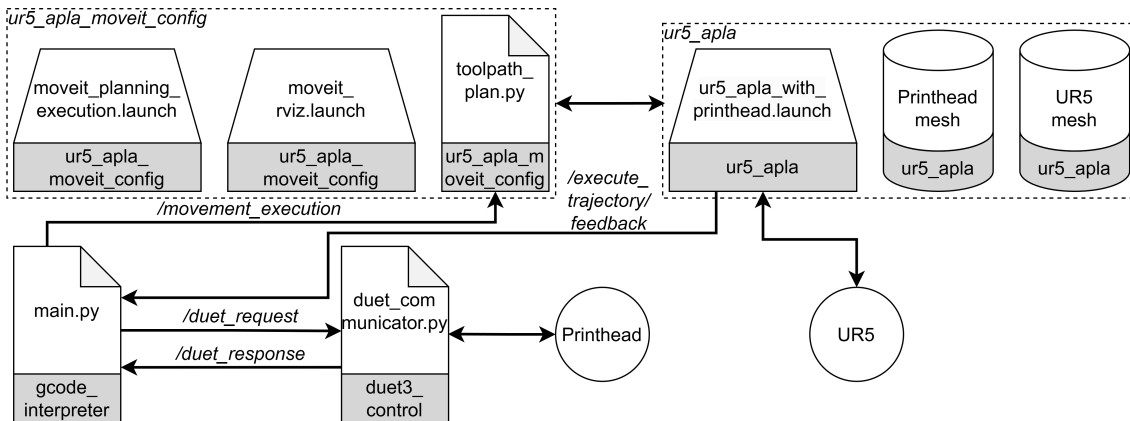
Figure 3.8: The ROS workflow during the printing process

After pre-processing, `main.py` maintains an ordered list of executable commands. Each command may include printing, motion, or both:

- Printing-only commands are sent via */duet_request*. The system waits for an acknowledgment on */duet_response* before proceeding.

- Movement-only commands are sent via */movement_execution*. The system remains idle for the pre-computed duration of robotic motion to be finished.

- Combined commands are more common. The pre-computed duration of robotic motion is used to time the corresponding extrusion precisely.

To avoid delays, consecutive movement commands are grouped. The G-code is structured in such a way that the first command in each group includes motion only. From the second command onward, the start time (published on */execute_trajectory/feedback*) and pre-computed durations allow accurate scheduling of printing instructions, ensuring that extrusion begins exactly when the robotic arm reaches the designated position.

3.2.2. G-code Creator

G-code (short for "Geometric Code") is the programming language used in Computer Numerical Control (CNC) and 3D printing to control movement and extrusion [34]. Standard slicers generate G-code by dividing Computer-Aided Design (CAD) models into layers, then producing instructions per layer. However, these tools are unsuitable for models which already contain pre-defined layers. Rather than re-slicing these models, the layers
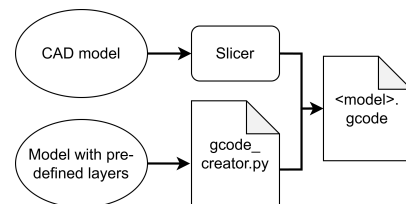

Figure 3.9: The workflow for creating a G-code file depending on your model input

are directly converted into G-code. To support this, a custom low-level tool was developed. It translates 2D isolines into G-code instructions suitable for thin-walled structures. The workflow is illustrated in Figure 3.10.

Both G-code creation workflows are suitable for the multi-axial printing system, as long as the created G-code contains valid instructions. These different workflows are depicted in Figure 3.9.
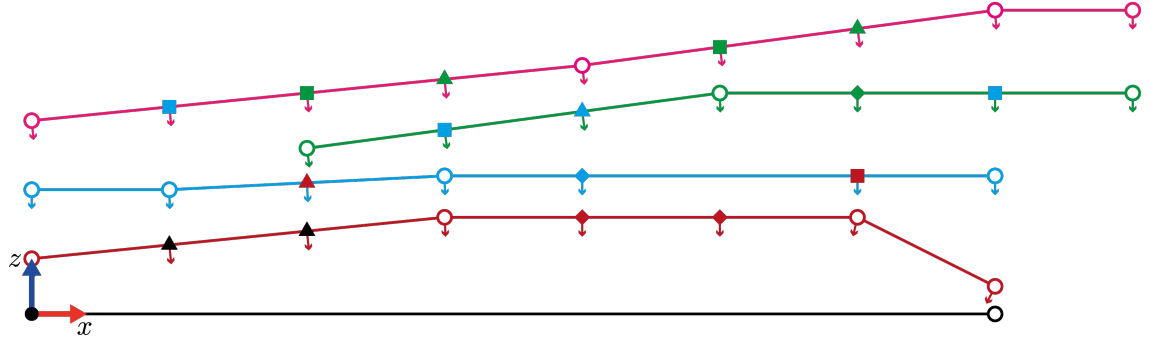
$$\mathcal{N}_{\text{seg}} = \{(x_k, y_k, \mathbf{n}_k, \ell) \mid k \in K, \ell \in L\}$$

$$\mathcal{S}_{\text{input}} = \{s_j = ((x_j^s, y_j^s), (x_j^e, y_j^e), \ell) \mid j \in J, \ell \in L\}$$
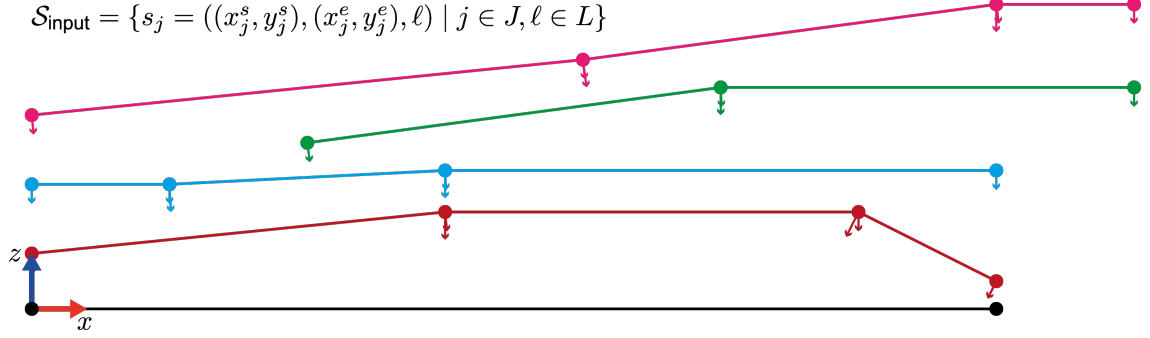
(a) Construction of segments from the input nodes, used to enrich each node with an inward-pointing normal vector.

$$\mathcal{N}_{\text{final}} = \mathcal{N}_{\text{beneath}} \cup \mathcal{N}_{\text{flow}} \cup \mathcal{N}_{\text{rotation}} \cup \mathcal{N}_{\text{merged}}$$

(b) Complete set of final nodes $\mathcal{N}_{\text{final}}$. $\mathcal{N}_{\text{beneath}}$ is shown as a square; $\mathcal{N}_{\text{flow}}$ as a triangle; $\mathcal{N}_{\text{rotation}}$ as a rhombus; and $\mathcal{N}_{\text{merged}}$ as a circle with a white infill.

$$\mathcal{I} = \left\{\mathcal{I}_k = \left(\mathbf{c}_1^k, \mathbf{c}_2^k, \mathbf{c}_3^k, \mathbf{c}_4^k, \mathbf{n}_a^k, \mathbf{n}_b^k, A_k, \ell\right) \mid k \in K, \ell \in L\right\}$$
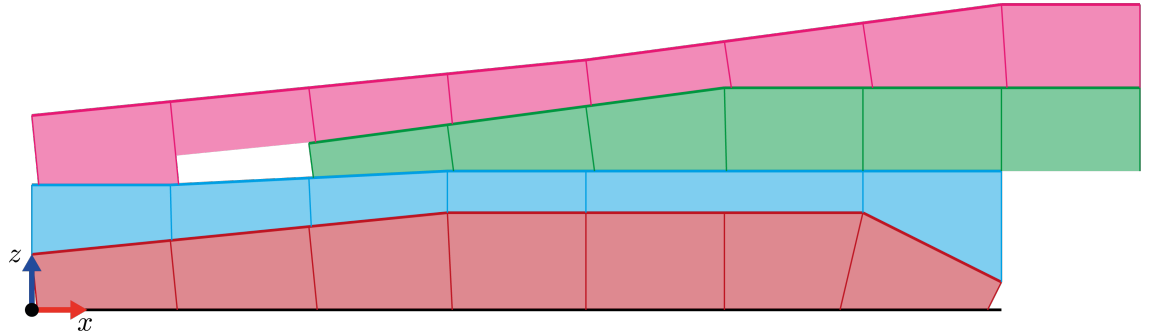
(c) Final visualisation showing all computed corners and areas. The internal separating lines implicitly indicate the direction of the inward normal vectors.

Figure 3.10: Visual summary of the G-code generation pipeline. Each subfigure illustrates a key step in the conversion from initial node-based input to final segment-based G-code instructions. Colours denote different isolines ℓ across all figures.

The G-code generator enables discretization according to either user-defined preferences or the constraints of the printing setup. In the present case, the system's communication bandwidth imposes a minimum discretization step size of 0.5 mm. Another important consideration in the design of the

G-code generator is the mitigation of local gouging, as illustrated in Figure 2.1. To address this, the nozzle path is designed to follow the local surface as closely as possible, thereby minimizing the risk of surface damage. The workflow that leads to the creation of the G-code instructions can be summarized in the following steps:

1. A set of initial nodes, $\mathcal{N}_{\text{input}} = \{(x_i, y_i, \ell) \mid i \in I, \ell \in L\}$ is received, where each node contains its 2D coordinates and associated isoline index.

2. From the input nodes, a set of linear segments is generated, $\mathcal{S}_{\text{input}} = \{s_j = ((x_j^s, y_j^s), (x_j^e, y_j^e), \ell) \mid j \in J, \ell \in L\}$. Each segment connects a pair of points along a common isoline ℓ.

3. Using the start and end point of each segment, the corresponding nodes are enriched with an inward-facing normal vector. Due to the non-continues nature of the line segments, several nodes may share the same coordinates but differ in their normals. The enriched node set is defined by $\mathcal{N}_{\text{seg}} = \{(x_k, y_k, \mathbf{n}_k, \ell) \mid k \in K, \ell \in L\}$. The segments and their corresponding enriched nodes are visualised in Figure 3.10a, where the direction of the normal is indicated by an arrow and each colour represents a different isoline ℓ.

4. Additional nodes are introduced by evaluating segments that lie directly beneath existing segments. If such segments contain nodes not yet present above, new nodes are created at corresponding positions and normals. This results in the additional node set $\mathcal{N}_{\text{beneath}}$ and a corresponding segment set $\mathcal{S}_{\text{beneath}}$.

5. Further refinement is carried out on $\mathcal{S}_{\text{beneath}}$ by comparing the gradient to the segment directly below it. If the segments have a different gradient, intermediate nodes are inserted at regular intervals in $\mathcal{N}_{\text{flow}}$, defined by the discretisation step $x_{disc} = 0.5$ mm.

6. To capture rotational features along longer segments in $\mathcal{S}_{\text{input}}$, additional nodes are inserted if the horizontal extent of a segment satisfies $x_j^e - x_j^s \geq 3x_{disc}$. Nodes are added at $x_j^s + x_{disc}$ and $x_j^e - x_{disc}$, provided no existing nodes are already present at these locations. The resulting set is denoted as $\mathcal{N}_{\text{rotation}}$.

7. Many nodes in $\mathcal{N}_{\text{seg}}$ occupy identical coordinates but have differing normals. These overlapping nodes are merged by averaging their normal vectors, yielding $\mathcal{N}_{\text{merged}}$. The final node set is constructed by combining all relevant sets, $\mathcal{N}_{\text{final}} = \mathcal{N}_{\text{beneath}} \cup \mathcal{N}_{\text{flow}} \cup \mathcal{N}_{\text{rotation}} \cup \mathcal{N}_{\text{merged}}$. The complete set of all relevant nodes is visualised in Figure 3.10b.

8. Using the nodes in $\mathcal{N}_{\text{final}}$, the final segment set in $\mathcal{S}_{\text{final}}$ is constructed. For each node, a ray is traced in the direction of its normal vector. The intersection of this ray with a segment below is computed and designated as a corner point for the extrusion region.

9. With the computed corner points, the area of each region between segments is determined. This area is used to calculate the amount of filament to be extruded. The final output is illustrated in Figure 3.10c, and the complete set of instructions is denoted by:

$$\mathcal{I} = \left\{ \mathcal{I}_k = \left(\mathbf{c}_1^k, \mathbf{c}_2^k, \mathbf{c}_3^k, \mathbf{c}_4^k, \mathbf{n}_a^k, \mathbf{n}_b^k, A_k, \ell \right) \mid k \in K, \ell \in L \right\},$$

where each instruction $\mathcal{I}_k$ comprises:

- $\mathbf{c}_i^k \in \mathbb{R}^2$ the four corner coordinates in clockwise order,

- $\mathbf{n}_a^k, \mathbf{n}_b^k \in \mathbb{R}^2$ the normal vectors of the top segment nodes,

- $A_k \in \mathbb{R} \geq 0$ the area of the segment's region,

- $\ell \in L$ the corresponding isoline index.

Additional pre- and post-processing steps are implemented to ensure safe transitions between layers and to prevent collisions during printing. For instance, an additional z-translation is applied at the end of each layer, lifting the nozzle tip clear of the printed object before moving to the starting position of the next layer. To enhance printability, the generated instructions are duplicated with a slight offset in the y-direction. This approach increases the overall thickness of the model, thereby improving structural stability and providing better support for greater build heights.

4

Results

This chapter presents the results of various tests conducted using the multi-axial printing setup. The goal is to explore and quantify the geometric limitations of non-planar printing. In section 4.1 the test setup and findings for a local geometric constraint is discussed, while section 4.2 addresses a global geometric limitation. Lastly, several nodal models are printed and analysed in section 4.3, serving to validate the findings from the previous sections.

All tests were conducted using polylactic acid (PLA) and a given printing speed of 600 mm/min. The nozzle temperature remains constant during printing at 200 °C.

4.1. Local slope test

The objective of the local slope test is to determine the maximum achievable slope within a single layer, referred to as "local", without compromising the intended geometry. Each test is performed with and without printhead rotation. When rotation is enabled, the printhead is oriented along the surface normal of the path; when disabled, the printhead remains normal to the printing platform.

4.1.1. Path input

The G-code Creator, see subsection 3.2.2, was used to generate a toolpath. A consistent base is established by depositing three planar layers. The fourth layer introduces a slope, transitioning from the maximum layer height, 0.35 mm, to the minimum, 0.1 mm, as illustrated in Figure 4.1.
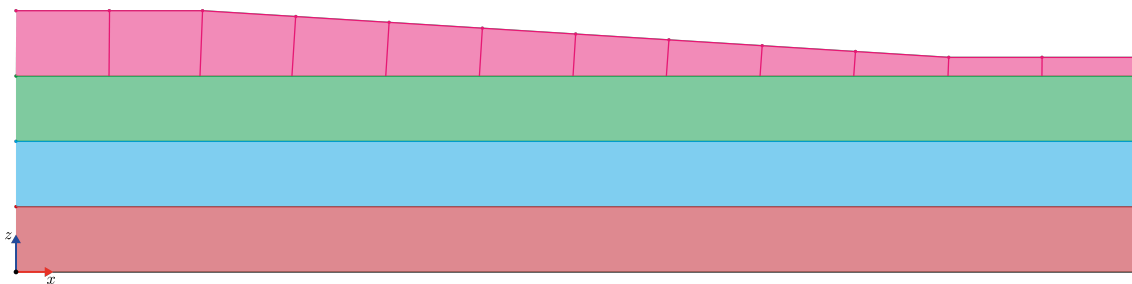

Figure 4.1: Cross-sectional view of the print path for the local slope test.

Flow rate is adjusted every 0.5 mm along the x-axis, while rotation, if enabled, occurs gradually over a 1 mm span, beginning 0.5 mm before the slope. This ensures the printhead remains perpendicular to the path for as long as possible. The distance between the highest and lowest layer height is reduced in successive tests, increasing the slope.

Each print sequence of the final layer can be described by five distinct phases:

- **Phase 1**: A steady-state extrusion for a planar layer at maximum height. For a total distance of approximately 100 mm.
- **Phase 2**: A 1 mm rotation from vertical to slope-normal orientation (if enabled).
- **Phase 3**: Constant orientation while adjusting flow rate every 0.5 mm.
- **Phase 4**: A return rotation to vertical orientation over 1 mm (if enabled).
- **Phase 5**: The layer is finished with a steady-state extrusion again. This time for a planar layer at minimum height.

4.1.2. Results with rotation

Figure 4.2 presents the micrographs of tests with printhead rotation. Red arrows mark the intended slope region. Rotation is initiated 0.5 mm before and ends 0.5 mm after this region.

(a) Distance 10 mm, angle of $1.4°$ w.r.t. z-axis.

(b) Distance 5 mm, angle of $2.9°$ w.r.t. z-axis.

(c) Distance 2 mm, angle of $7.1°$ w.r.t. z-axis.

(d) Distance 1 mm, angle of $14.0°$ w.r.t. z-axis.
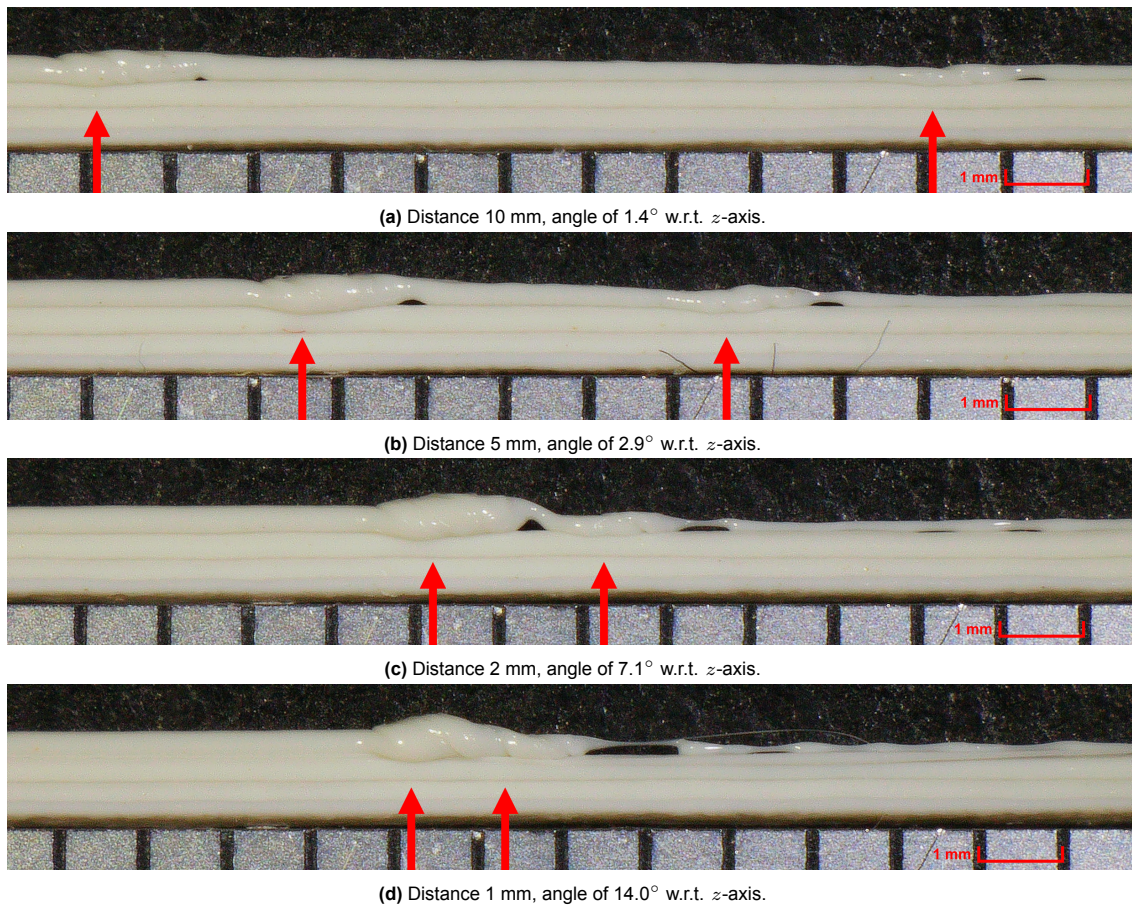
Figure 4.2: Micrographs of the local slope test with rotation. The red arrow indicates the start and end point of the introduced slope.

4.1.3. Results without rotation

Figure 4.3 shows results without rotation. Although no rotation occurs, the path remains segmented as in Figure 4.1. For the steepest slopes, Figure 4.3d and 4.3e, a blue arrow marks the actual end point of the slope, which deviates from the intended location.
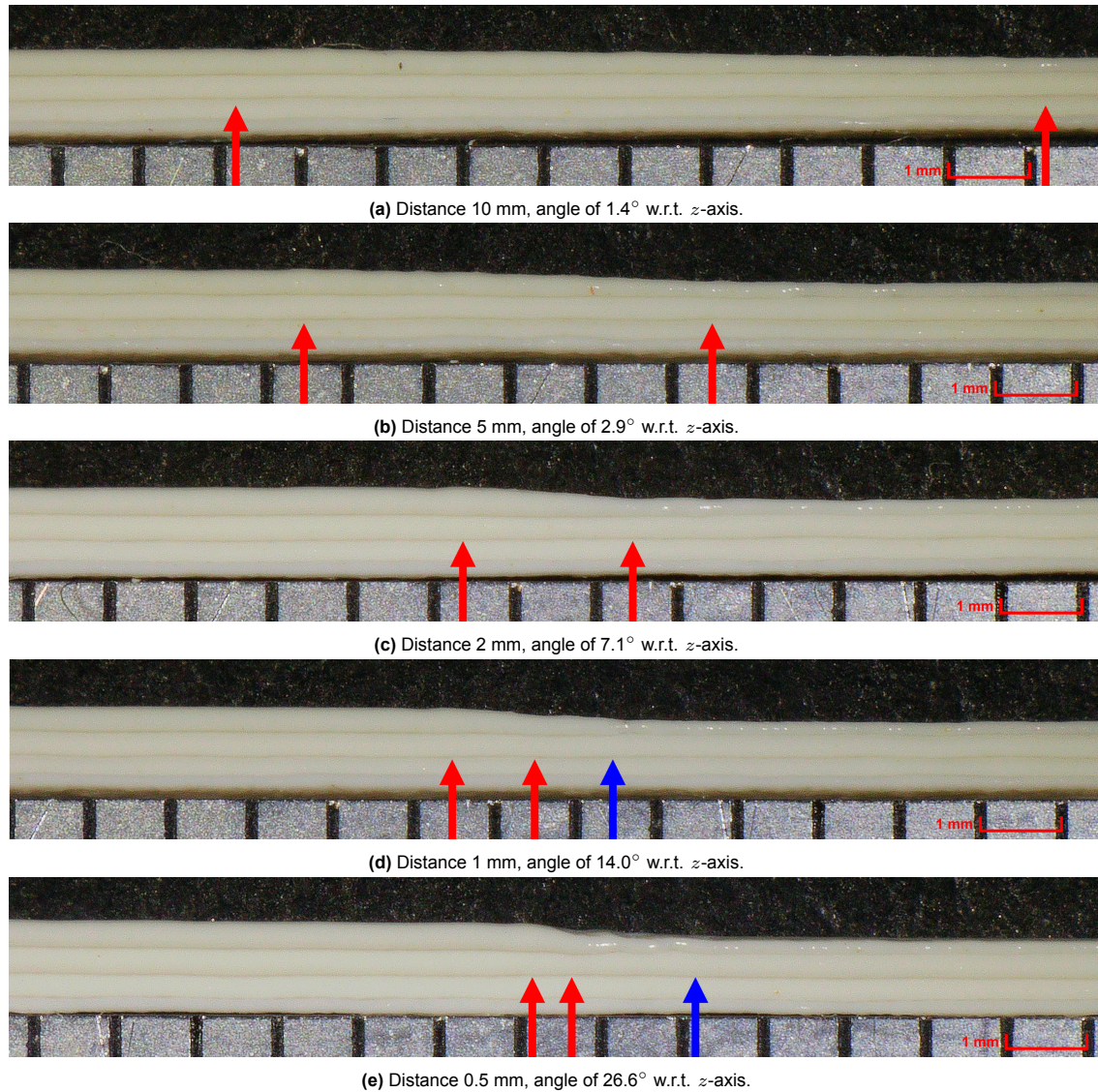

(a) Distance 10 mm, angle of 1.4° w.r.t. z-axis.

(b) Distance 5 mm, angle of 2.9° w.r.t. z-axis.

(c) Distance 2 mm, angle of 7.1° w.r.t. z-axis.

(d) Distance 1 mm, angle of 14.0° w.r.t. z-axis.

(e) Distance 0.5 mm, angle of 26.6° w.r.t. z-axis.

Figure 4.3: Micrographs of the local slope test without rotation. The red arrow indicates the start and end point of the introduced slope. The blue arrow, if present, indicates the observed end point of the introduced slope.

4.1.4. Quantitative Comparison

To better compare the differences between the tests, the slope region is normalised to begin at 0 mm. Flow rate vs. distance and flow rate vs. time plots are shown in Figure 4.4 for several slopes.

(a) Flow rate at each increment for a slope of $1.4°$ over 10 mm.

(b) Duration of each flow rate for a slope of $1.4°$ over 10 mm.

(c) Flow rate at each increment for a slope of $2.9°$ over 5 mm.

(d) Duration of each flow rate for a slope of $2.9°$ over 5 mm.

(e) Flow rate at each increment for a slope of $7.1°$ over 2 mm.

(f) Duration of each flow rate for a slope of $7.1°$ over 2 mm.

(g) Flow rate at each increment for a slope of $14.0°$ over 1 mm.

(h) Duration of each flow rate for a slope of $14.0°$ over 1 mm.

Figure 4.4: Several figures showing the relation between flow rate, time and location of the several tests.

4.1.5. Discussion

The micrographs presented in Figure 4.2 and 4.3 indicate that enabling printhead rotation introduces notable defects, particularly at the start and end of the slope. These defects align with regions where the printhead undergoes re-orientation.

An analysis of Figure 4.4a, 4.4c, and 4.4e shows that the flow rate is significantly reduced during the re-orientation phase. This reduction is also observed in the corresponding time-domain plots, Figure 4.4b, 4.4d, and 4.4f. These plots reveal that the low-flow intervals are prolonged, reflecting the time-intensive nature of re-orienting the nozzle in the multi-axial printing setup.

The graphs clearly indicate that during reorientation, the UR5 is unable to maintain the target travel velocity of 600 mm/min. Due to the reduced velocity in segments involving reorientation commands, the duration of material extrusion must be extended. Consequently, the flow rate must be decreased to ensure that the total extruded volume remains accurate.

In theory, the reduced flow rate should compensate for the longer duration. However, the results in Figure 4.2 suggest otherwise. The observed over-extrusion implies that the actual flow rate during re-orientation exceeds the intended value. This discrepancy is likely due to the residual behaviour of material extrusion: even when the extruder motor halts, molten filament remains in the heated zone and may continue to flow due to gravity, inertia, or internal pressure. The extended duration of nozzle re-orientation intensifies this effect, resulting in the localised over-extrusion which can be observed in Figure 4.2.

The excess extrusion is typically followed by a region of under-extrusion. This phenomenon can be explained by the mechanics of filament feeding: during over-extrusion, the feeding tube between the extruder and the nozzle becomes partially depleted. Consequently, when the extruder resumes at a higher flow rate, it initially replenishes the empty section of the tube rather than depositing material onto the print surface. This leads to a temporary shortfall in material deposition, resulting in under-extrusion.

In contrast, the tests conducted without rotational movements, as shown in Figure 4.3, demonstrate more consistent material deposition. In these cases, the UR5 is able to maintain the target travel velocity of 600 mm/min, allowing for gradual reductions in flow rate solely due to the decreasing volume requirements. This allows the system to maintain a seeming steady-state condition, minimising disruptions in extrusion behaviour.

Furthermore, it can be seen in Figure 4.3d and 4.3e that the slope extends beyond the intended region. For both the 1 mm and 0.5 mm tests, the transition occurs over approximately 2 mm. This suggests that the actual flow rate may exceed the planned value, and that a transition of 39 mm/min over 0.3 seconds may be too abrupt for the system to handle accurately.

Comparing Figure 4.3d to Figure 4.3e, a clear difference in print quality is observed. The 1 mm test resembles the 2 mm case, possibly due to residual flow aligning more closely with the intended path. In contrast, the 0.5 mm test exhibits significant distortion at the intended slope endpoint. This may be due to the nozzle tip interfering with the previously over-deposited material, dragging it along the surface and further distorting the geometry.

The local slope tests clearly indicate that the observed defects result from a high temporal gradient in the flow rate. This pronounced gradient often arises because the UR5 is unable to maintain a consistent velocity during rotational movements. Only at high geometric slopes, specifically 14.0° or 26.6°, do the required flow rate adjustments become excessive due to the significant volumetric changes in the deposited layer.

4.2. Global slope test

The global slope test is designed to evaluate the maximum surface inclination on which material can be reliably deposited during non-planar printing. This test is sensitive to material-specific characteristics, such as viscosity and the rate of solidification upon extrusion. To isolate the effect of surface inclination, no local slope variations are introduced within individual layers. Each layer is therefore deposited at a constant flow rate.

4.2.1. Path input

The print path for the global slope test consists of two distinct phases. In the first phase, an inclined surface is constructed using layers of uniform height, ensuring a continuous and consistent material flow. The second phase involves depositing additional layers on top of the inclined surface, progressing from the base of the inclination to its peak.

An exception was made for the 90° inclination test. After the initial five layers were printed from bottom to top, the deposition direction was reversed to top to bottom for the subsequent five layers. Throughout the test, the printhead remains oriented normal to the surface, maintaining consistent alignment with the incline. A representative cross-sectional view of the path input for a 50° inclination is shown in Figure 4.5.

Figure 4.5: Toolpath around the incline for the global slope test.

4.2.2. Results

The global slope test was performed for surface inclinations of 50°, 60°, 70°, 80°, and 90°. Micrographs of the resulting prints illustrate the quality of material deposition at each inclination. A selection of results, including 50°, 70°, and 90° inclinations, is shown in Figure 4.6. The complete set of images can be found in Appendix B.

(a) Inclination of 50°.

(b) Inclination of 70°.

(c) Inclination of 90°.
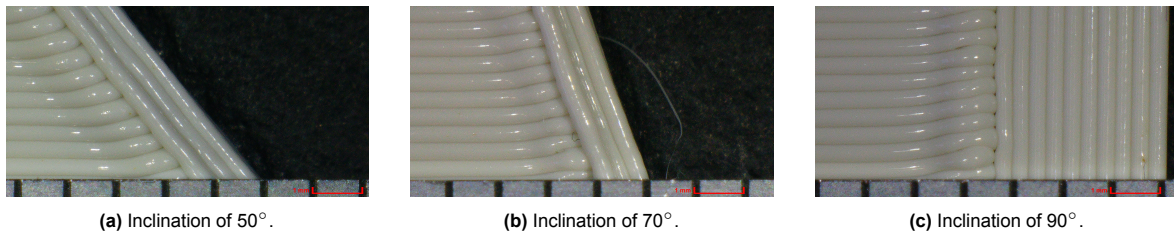
Figure 4.6: Micrographs of the deposited layers on an inclined surface.

4.2.3. Discussion

The images in Figure 4.6 demonstrate that the multi-axial printing setup is capable of depositing material reliably on steep inclined surfaces. Across all tested angles, including the extreme case of 90°, there is no evident loss of adhesion or deformation of the printed layers. This indicates that the material remains sufficiently stable during deposition to maintain its intended geometry.

Notably, even for the vertical inclination of 90°, the change in deposition direction does not negatively impact the quality of the printed surface. This suggests that, under the given conditions, the deposition direction is not a critical factor for layer integrity at high inclines.

These results imply that the PLA used in this test solidifies rapidly enough upon extrusion to prevent flow or sagging, even on vertical surfaces.

4.3. Full model test

Based on the results from section 4.1 and 4.2, it can be concluded that the quality of non-planar printing is strongly influenced by variations in flow rate, which are in turn governed by the time required to move

between successive points along the toolpath. It is therefore expected that gradual transitions and smooth motions tend to result in better material deposition and overall print quality.

To assess these effects in practice, three L-brackets were printed using different slicing strategies: one with planar layers (as a reference), one with multiplanar layers [35], and one with fully non-planar layers using the STTO approach [36]. The results of these prints are presented in this section.

4.3.1. Path input
The toolpaths used for each model vary considerably, as visualised in Figure 4.7. Each slicing method introduces its own key challenges. For the planar model, the main point of concern is the unsupported overhang at the lower-right edge of the bracket. In the multi-planar model, attention is focused on the junction between segments printed at different orientations. For the STTO model, the point of interest lies in the gradual gradient transitions across the print. Close-up view of each toolpath around these critical areas are provided in Figure 4.7 as well.

(a) The planar L bracket.   **(b)** The multiplanar L bracket.   **(c)** The STTO L bracket.
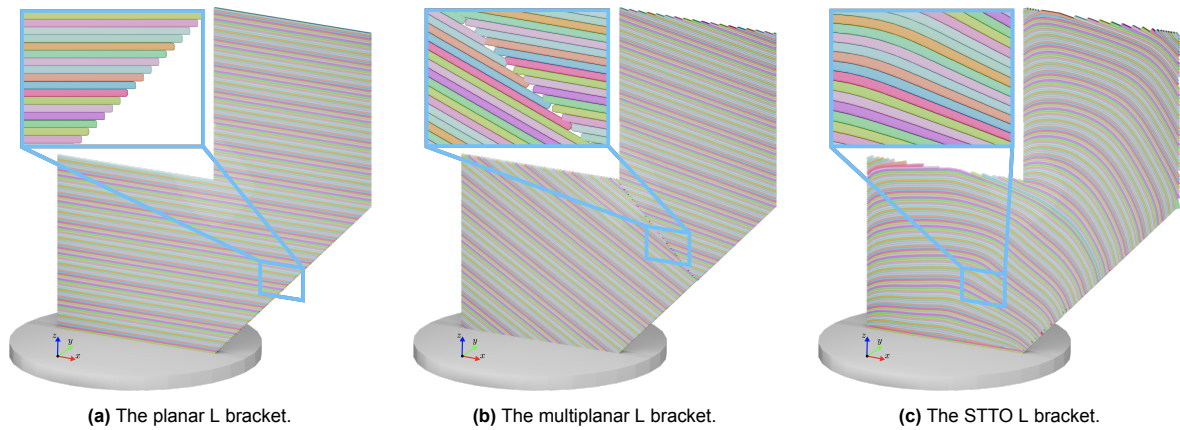
Figure 4.7: Overview of the toolpaths for several models of the L bracket. A close-up of each point of interest is included.

4.3.2. Results
The outcomes of each print are shown in Figure 4.8. Some inconsistencies are present due to the distance of 2 meters between the filament spool and extruder. Because of this distance a lot of friction is present in the filament tube. This sometimes causes the extruder to slip over the filament, resulting in excess or insufficient material deposition. These defects are not considered in the evaluation, since they are not caused by the toolpath, which is what will be examined in these tests. A detailed view of each model's critical region is provided in Figure 4.9.

(a) The planar L bracket.   **(b)** The multiplanar L bracket   **(c)** The STTO L bracket
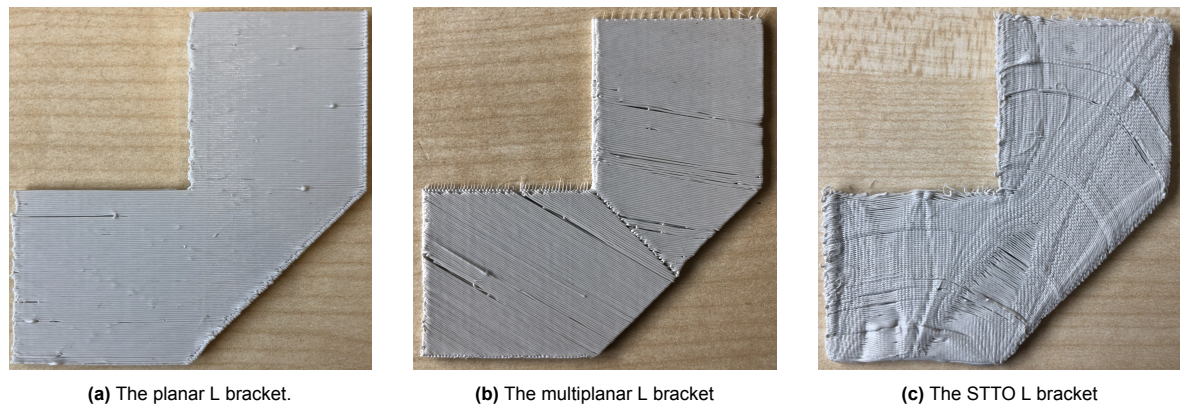
Figure 4.8: Pictures of the print results for several models of the L bracket.

(a) The planar L bracket.   (b) The multiplanar L bracket.   (c) The STTO L bracket.
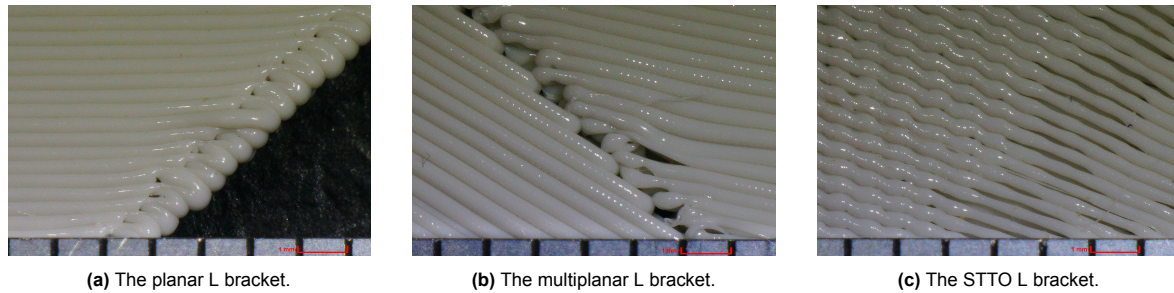
Figure 4.9: Micrographs of the point of interest of each L bracket.

4.3.3. Discussion

As seen in Figure 4.8, the overall print quality across all three L brackets is satisfactory, with no major defects or structural failures. However, each slicing strategy presents its own challenges.

In the planar model, the unsupported overhang causes the filament to sag, as shown in Figure 4.9a. The last 0.15 mm of each layer along the overhang lacks sufficient support during deposition, which has caused the filament to sag. This sagging may have induced a slight over-extrusion effect, as the viscosity of the filament could draw out additional material during the unsupported span.

The multi-planar model, Figure 4.8b, resolves the overhang issue by reorienting the layers, reducing the effective angle of the overhang to approximately 15 degrees relative to the build direction. This leads to significantly improved edge definition and surface finish. However, a discontinuity and defects appear at the transition between the two print segments with differing orientations. This offset likely stems from a cumulative alignment deviation along the print boundary, which becomes more apparent due to the reorientation of layers. A similar deviation can also be observed on the outer edge of the planar model. A closer examination of the partition area, as shown in Figure 4.9b, reveals the presence of a pronounced staircase effect along this region. This effect results from the layers being terminated at an angle that differs from their primary orientation, leading to significant discretisation. Although the layers attempt to interlock, this is not always achieved successfully, resulting in numerous gaps within the partition area. These gaps indicate a structural weakness in the overall multiplanar model when fabricated using ME.

The final model, produced using the STTO method, incorporates continuous variation in orientation and layer height, with each 0.5 mm segment printed at a new configuration. At first glance, this would appear problematic due to the flow rate instability observed in section 4.1. However, since nearly all segments involve reorientation, the velocity is reduced consistently across most segments. This uniform reduction in velocity, in turn, leads to the average flow rate remaining in a near steady-state condition. As a result, the STTO model was successfully printed.

Nonetheless, local flow rate fluctuations are still visible. In Figure 4.8c and Figure 4.9c, the printed line width varies across different sections. Areas with gradients result in closely packed, slightly over-extruded segments, while flatter regions allow for faster printhead movement and appear under-extruded. This behaviour directly reflects the results of the local gradient test discussed previously.

The model tests indicate that the toolpaths, whether multiplanar or STTO, already fall within the printable limits. Consequently, it is likely that these models can be manufactured using a multi-axial WAAM setup. The defects observed along the partition of the multiplanar model may also be mitigated in this context, as the DED process used in WAAM involves material pooling, which can close such gaps. Similarly, the over- and under-extrusion issues identified in the STTO model are expected to be reduced when using WAAM. Unlike ME, WAAM does not suffer from residual flow issues, as the material is not pre-melted but is only melted at the point of deposition.

5

Conclusion

Recent advancements in multi-axial robotic additive manufacturing have enabled non-planar deposition, introducing a new design freedom: the shape and sequence of individual layers during fabrication. This additional degree of freedom has been the cornerstone of several developments in additive manufacturing, where curved layers and their deposition sequences are modified for various optimisation purposes. However, although non-planar layers have already been successfully produced, the fundamental constraints that define the geometrical limits of curved-layer deposition have not yet been systematically established. The objective of this thesis was therefore to identify these limits for non-planar printing.

To investigate these boundaries, this research presented the development of a custom multi-axial robotic printing setup, designed in consideration of constraints identified in the literature. In addition, a two-dimensional toolpath generator was developed to produce customised instructions for the setup, enabling precise control of the experimental conditions.

This thesis has demonstrated that, apart from collision avoidance, the primary limitation of curved-layer deposition is the discrepancy between the actual and intended flow rate. Large variations, either increasing or decreasing, were found to cause deviations from the intended geometry, primarily due to the intrinsic dynamics of the extrusion process. Since material extrusion relies on a steady-state flow to ensure consistent deposition, large sudden changes in flow rate can lead to under- or over-extrusion.

It was found that pronounced gradients in flow rate arise either from inconsistent velocity of the multi-axial setup or from excessive volumetric changes in the deposited material. The latter behaviour was observed to occur at layer height changes of $14.0°$ or greater.

Further validation was performed through full-scale tests on two larger models, each designed with different limits tailored to specific optimisation objectives in Wire-Arc Additive Manufacturing (WAAM). Despite the identified limitations, these models were printed with promising results, as their gradual curvature resulted in relatively consistent flow rates. Since WAAM employs a different extrusion mechanism, where the material is only melted at the point of deposition and steady-state flow rate is less critical, it is hypothesised that such layer changes would introduce fewer defects in WAAM compared to the used Material Extrusion method. This hypothesis provides a valuable starting point for future experimental studies.

6

Recommendations

The presented work has provided insight into the fundamental manufacturing constraints that define the feasible domain for curved-layer deposition. It has been demonstrated that the geometrical constraints are strongly influenced by the temporal gradient in flow rate. Through the use of continuous, segmented paths which minimise sudden flow changes, it is possible to fabricate complex geometries with adequate resemblance of the intended model. However, several areas could benefit from further investigation to improve the reliability and quality of non-planar additive manufacturing. These areas will be discussed in this chapter.

First, the presented two-dimensional toolpath generator calculates deposition paths based on the central axis of the nozzle, without accounting for the nozzle's diameter. This simplification introduces discrepancies between the theoretical toolpath and the actual deposited material. Specifically, the deposited path extends laterally by approximately half the nozzle diameter on either side, resulting in under-extrusion across individual segments and potential over-extrusion at path intersections due to overlapping deposition. A more accurate nozzle representation in the toolpath computation could help reduce these geometric inaccuracies.

Second, improving control over the actual filament flow is critical. The experimental results have revealed that the intended and actual flow rates are often misaligned due to the intrinsic dynamics of the extrusion process. Further research into modelling and compensating for residual flow effects could allow for better flow instructions. Adaptive control strategies that modulate flow in response to predicted or sensed deviation could be explored in this context.

Third, optimisation of the layer paths to maintain a low temporal gradient in flow rate requires precise knowledge of the travel time along a given toolpath. In the current setup, discrepancies arise during rotational movements due to how the velocity is interpreted by the inverse kinematics solver. By incorporating this interpretation into the optimisation it would become possible to also optimise the geometry of the layer with the additional objective to minimise sudden flow rate changes. This will must likely result in less discrepancies between the theoretical toolpath and the actual deposited material.

Fourth, it is hypothesised that the flow rate constraints observed in this research may not be applicable to other AM techniques, such as DED. To extend the applicability of this research to WAAM, a comparative analysis is needed to evaluate the similarities and differences in deposition dynamics between ME and DED. In order to use the developed custom multi-axial robotic printing setup as a reference for WAAM further research needs to be conducted to define the similarities and differences between the ME and DED technique.

Lastly, a significant direction for future research is the extension of the current toolpath generation framework to support full three-dimensional path planning. Enhancing the tool to generate instructions for predefined, spatially curved layers would enable the utilisation of the multi-axial printing setup in all six degrees of freedom.

References

[1] W. Gao, Y. Zhang, D. Ramanujan, *et al.*, "The status, challenges, and future of additive manufacturing in engineering," *Computer-Aided Design*, vol. 69, pp. 65–89, Apr. 2015. DOI: `10.1016/j.cad.2015.04.001`. [Online]. Available: `https://doi.org/10.1016/j.cad.2015.04.001`.

[2] T. D. Ngo, A. Kashani, G. Imbalzano, K. T. Nguyen, and D. Hui, "Additive manufacturing (3D printing): A review of materials, methods, applications and challenges," *Composites Part B Engineering*, vol. 143, pp. 172–196, Feb. 2018. DOI: `10.1016/j.compositesb.2018.02.012`. [Online]. Available: `https://doi.org/10.1016/j.compositesb.2018.02.012`.

[3] S. C. Costello, C. R. Cunningham, F. Xu, A. Shokrani, V. Dhokia, and S. T. Newman, "The state-of-the-art of wire arc directed energy deposition (WA-DED) as an additive manufacturing process for large metallic component manufacture," *International Journal of Computer Integrated Manufacturing*, vol. 36, no. 3, pp. 469–510, Jan. 2023. DOI: `10.1080/0951192x.2022.2162597`. [Online]. Available: `https://doi.org/10.1080/0951192x.2022.2162597`.

[4] S. W. Williams, F. Martina, A. C. Addison, J. Ding, G. Pardal, and P. Colegrove, "Wire + Arc Additive Manufacturing," *Materials Science and Technology*, vol. 32, no. 7, pp. 641–647, May 2015. DOI: `10.1179/1743284715y.0000000073`. [Online]. Available: `https://doi.org/10.1179/1743284715y.0000000073`.

[5] W. Wang, K. Wu, V. K. Fred, and J. Wu, "Regularization in Space-Time topology optimization for Multi-Axis additive manufacturing," *arXiv (Cornell University)*, Apr. 2024. DOI: `10.48550/arxiv.2404.13059`. [Online]. Available: `https://arxiv.org/abs/2404.13059`.

[6] K. Treutler and V. Wesling, "The Current State of Research of Wire Arc Additive Manufacturing (WAAM): A review," *Applied Sciences*, vol. 11, no. 18, p. 8619, Sep. 2021. DOI: `10.3390/app11188619`. [Online]. Available: `https://doi.org/10.3390/app11188619`.

[7] F. Xu, V. Dhokia, P. Colegrove, *et al.*, "Realisation of a multi-sensor framework for process monitoring of the wire arc additive manufacturing in producing Ti-6Al-4V parts," *International Journal of Computer Integrated Manufacturing*, vol. 31, no. 8, pp. 785–798, Apr. 2018. DOI: `10.1080/0951192x.2018.1466395`. [Online]. Available: `https://doi.org/10.1080/0951192x.2018.1466395`.

[8] T. A. Rodrigues, V. Duarte, R. M. Miranda, T. G. Santos, and J. P. Oliveira, "Current status and perspectives on Wire and Arc Additive Manufacturing (WAAM)," *Materials*, vol. 12, no. 7, p. 1121, Apr. 2019. DOI: `10.3390/ma12071121`. [Online]. Available: `https://doi.org/10.3390/ma12071121`.

[9] C. Zhang, C. Shen, X. Hua, F. Li, Y. Zhang, and Y. Zhu, "Influence of wire-arc additive manufacturing path planning strategy on the residual stress status in one single buildup layer," *The International Journal of Advanced Manufacturing Technology*, vol. 111, no. 3-4, pp. 797–806, Oct. 2020. DOI: `10.1007/s00170-020-06178-w`. [Online]. Available: `https://doi.org/10.1007/s00170-020-06178-w`.

[10] J. Zhu, H. Zhou, C. Wang, L. Zhou, S. Yuan, and W. Zhang, "A review of topology optimization for additive manufacturing: Status and challenges," *Chinese Journal of Aeronautics*, vol. 34, no. 1, pp. 91–110, Oct. 2020. DOI: `10.1016/j.cja.2020.09.020`. [Online]. Available: `https://doi.org/10.1016/j.cja.2020.09.020`.

[11] M. Bi, P. Tran, and Y. M. Xie, "Topology optimization of 3D continuum structures under geometric self-supporting constraint," *Additive manufacturing*, vol. 36, p. 101 422, Jun. 2020. DOI: `10.1016/j.addma.2020.101422`.

[12] J. R. Kubalak, A. L. Wicks, and C. B. Williams, "Exploring multi-axis material extrusion additive manufacturing for improving mechanical properties of printed parts," *Rapid Prototyping Journal*, vol. 25, no. 2, pp. 356–362, Nov. 2018. DOI: `10.1108/rpj-02-2018-0035`. [Online]. Available: `https://doi.org/10.1108/rpj-02-2018-0035`.

[13] W. Wang, D. Munro, C. C. L. Wang, F. Van Keulen, and J. Wu, "Space-time topology optimization for additive manufacturing," *Structural and Multidisciplinary Optimization*, vol. 61, no. 1, pp. 1–18, Nov. 2019. DOI: `10.1007/s00158-019-02420-6`. [Online]. Available: `https://doi.org/10.1007/s00158-019-02420-6`.

[14] K. Wu, F. Van Keulen, and J. Wu, "Residual stress-constrained space–time topology optimization for multi-axis additive manufacturing," *Computer Methods in Applied Mechanics and Engineering*, vol. 440, p. 117 913, May 2025. DOI: `10.1016/j.cma.2025.117913`. [Online]. Available: `https://doi.org/10.1016/j.cma.2025.117913`.

[15] R. Di Girolamo, *Layer thickness control in 3D fabrication sequence optimization for Multi-Axis additive manufacturing*, 2024. [Online]. Available: `http://resolver.tudelft.nl/uuid:486b73c5-8880-4838-ae47-59da715078ca`.

[16] L. Chen, M.-F. Chung, Y. Tian, A. Joneja, and K. Tang, "Variable-depth curved layer fused deposition modeling of thin-shells," *Robotics and Computer-Integrated Manufacturing*, vol. 57, pp. 422–434, Jan. 2019. DOI: `10.1016/j.rcim.2018.12.016`. [Online]. Available: `https://doi.org/10.1016/j.rcim.2018.12.016`.

[17] Y. Li, D. He, S. Yuan, K. Tang, and J. Zhu, "Vector field-based curved layer slicing and path planning for multi-axis printing," *Robotics and Computer-Integrated Manufacturing*, vol. 77, p. 102 362, Apr. 2022. DOI: `10.1016/j.rcim.2022.102362`. [Online]. Available: `https://doi.org/10.1016/j.rcim.2022.102362`.

[18] J. Etienne, N. Ray, D. Panozzo, *et al.*, "CurviSlicer," *ACM Transactions on Graphics*, vol. 38, no. 4, pp. 1–11, Jul. 2019. DOI: `10.1145/3306346.3323022`. [Online]. Available: `https://doi.org/10.1145/3306346.3323022`.

[19] T. Y. Lau, L. Chen, D. He, Z. Li, and K. Tang, "Partition-based print sequence planning and adaptive slicing for scalar field-based multi-axis additive manufacturing," *Computer-Aided Design*, vol. 163, p. 103 576, Jun. 2023. DOI: `10.1016/j.cad.2023.103576`. [Online]. Available: `https://doi.org/10.1016/j.cad.2023.103576`.

[20] T. Zhang, G. Fang, Y. Huang, *et al.*, "S 3 -Slicer," *ACM Transactions on Graphics*, vol. 41, no. 6, pp. 1–15, Nov. 2022. DOI: `10.1145/3550454.3555516`. [Online]. Available: `https://doi.org/10.1145/3550454.3555516`.

[21] Raise3D, *3D Printing Layer Height: Definition, Importance and Relationship with Nozzle Size – Raise3D: Reliable, Industrial Grade 3D Printer*. [Online]. Available: `https://www.raise3d.com/blog/3d-printing-layer-height/`.

[22] C. Dai, C. C. L. Wang, C. Wu, S. Lefebvre, G. Fang, and Y.-J. Liu, "Support-free volume printing by multi-axis motion," *ACM Transactions on Graphics*, vol. 37, no. 4, pp. 1–14, Jul. 2018. DOI: `10.1145/3197517.3201342`. [Online]. Available: `https://doi.org/10.1145/3197517.3201342`.

[23] Y. Yao, L. Cheng, and Z. Li, "A comparative review of multi-axis 3D printing," *Journal of Manufacturing Processes*, vol. 120, pp. 1002–1022, May 2024. DOI: `10.1016/j.jmapro.2024.04.084`. [Online]. Available: `https://doi.org/10.1016/j.jmapro.2024.04.084`.

[24] F. Hong, S. Hodges, C. Myant, and D. E. Boyle, "Open5x: Accessible 5-axis 3D printing and conformal slicing," *CHI Conference on Human Factors in Computing Systems Extended Abstracts*, pp. 1–6, Apr. 2022. DOI: `10.1145/3491101.3519782`. [Online]. Available: `https://doi.org/10.1145/3491101.3519782`.

[25] X. Wang, P. Fang, B. Teng, K. Xu, H. Sun, and X. Wang, *Design of WAAM system based on industrial robot*. Springer Nature Singapore, Dec. 2022, pp. 91–106. DOI: `10.1007/978-981-19-6149-6\{_}5`. [Online]. Available: `https://doi.org/10.1007/978-981-19-6149-6_5`.

[26] U. R. A/S, *UR5 Technical specifications*, 2016. [Online]. Available: `https://www.universal-robots.com/media/50588/ur5_en.pdf`.

[27] J. E. Colgate, M. A. Peshkin, and Individual, *US5952796A - CoBots - Google Patents*, Feb. 1996. [Online]. Available: `https://patents.google.com/patent/US5952796`.

[28] Duet, *Duet3D*. [Online]. Available: `https://www.duet3d.com/duet3mainboard6hc`.

[29] R. Lőrincz, *Orbiter v2.0 – ORBITER PROJECTS*. [Online]. Available: `https://www.orbiterprojects.com/orbiter-v2-0/`.

[30] E3D, *Revo Micro Documentation*. [Online]. Available: `https://e3d-online.zendesk.com/hc/en-us/articles/6450443315485-Revo-Micro-Documentation`.

[31] E3D, *Revo Support: Revo Nozzles*. [Online]. Available: `https://e3d-online.com/pages/revo-nozzle-datasheet`.

[32] Stanford Artificial Intelligence Laboratory et al., *Robotic operating system*, version ROS Noetic Ninjemys, May 23, 2020. [Online]. Available: `https://www.ros.org`.

[33] UniversalRobots, *Universal_robots_ros_driver*. [Online]. Available: `https://github.com/UniversalRobots/Universal_Robots_ROS_Driver`.

[34] K. Latif, A. Adam, Y. Yusof, and A. Z. A. Kadir, "A review of G code, STEP, STEP-NC, and open architecture control technologies based embedded CNC systems," *The International Journal of Advanced Manufacturing Technology*, vol. 114, no. 9-10, pp. 2549–2566, Apr. 2021. DOI: `10.1007/s00170-021-06741-z`. [Online]. Available: `https://doi.org/10.1007/s00170-021-06741-z`.

[35] V. Mishra and J. Wu, "Differentiable modelling and optimization of multi-planar slicing for multi-axis additive manufacturing," Manuscript submitted for publication, 2025.

[36] K. Wu, "Space-time topology optimization for multi-axis additive manufacturing," PhD dissertation, Delft University of Technology, 2025. DOI: `10.4233/uuid:3be97b56-f03e-4d07-b182-b1427f249db5`. [Online]. Available: `https://repository.tudelft.nl/record/uuid:3be97b56-f03e-4d07-b182-b1427f249db5`.

A
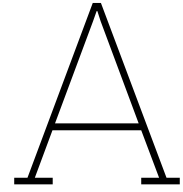
Printing Table

During preliminary tests, it was observed that the nozzle tip exhibited excessive vibrations during movements of the robotic arm. These vibrations led to noticeable imprecision in material deposition. To address this issue, the table on which the UR5 was mounted was reinforced using additional trusses and angled profiles. To quantify the effect of these modifications, several measurements were performed.

The test was conducted by mounting a pencil at the end of the print head. The pencil was calibrated to maintain a gap equal to the thickness of a sheet of paper above the printing platform. Vibrations would cause the pencil to occasionally contact the paper, leaving visible marks.

A square path, including infill, was used as the test trajectory. The extent of vibration was quantified by counting the number of contact marks the pencil left on the paper. The results of this experiment are shown in Figure A.1.

These results clearly demonstrate that the modifications to the printing table significantly reduced the vibrations. The test also revealed slight unevenness in the printing platform in certain areas. However, this deviation in flatness is smaller than the minimum layer thickness and is therefore compensated after the deposition of the first layer.

(a) Contact points observed during the square test before reinforcing the printing table.

(b) Contact points observed during the square test after reinforcing the printing table.
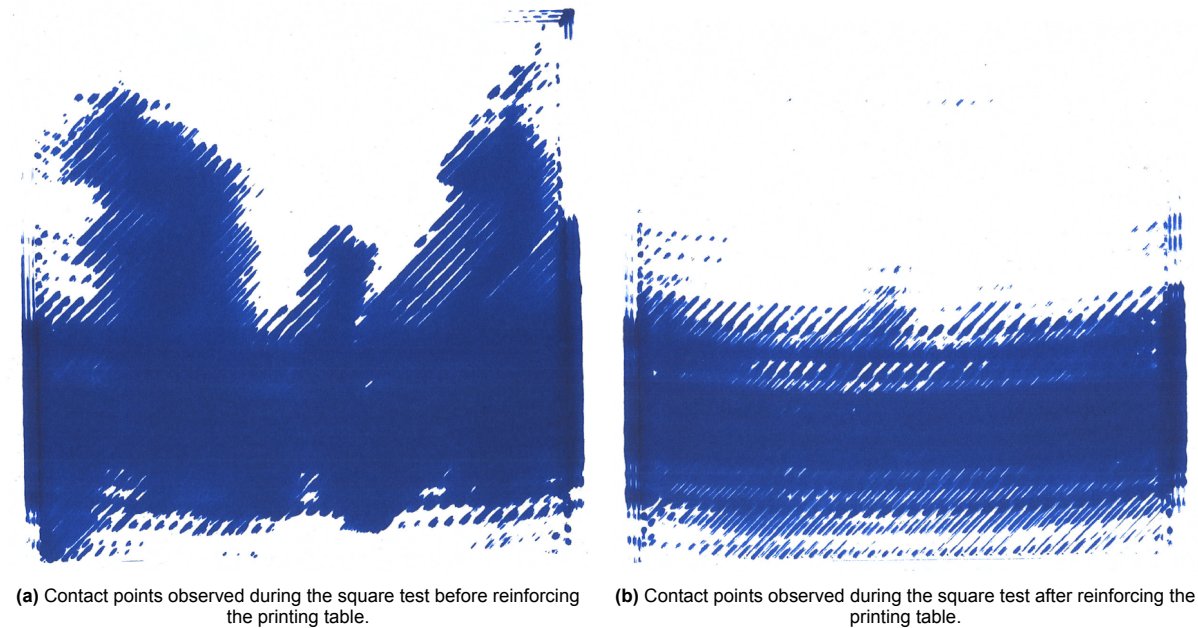
Figure A.1: Comparison of contact points recorded during the square test using a pencil attached to the print head, before and after reinforcing the printing table. Fewer contact points indicate reduced vibrations.

B

Elaborate results

All results regarding the local slope test, section 4.1, and the global slope test, section 4.2, are shown in this Appendix. Figure B.1, B.2 and B.3 show all the results of the local slope test and Figure B.4 shows all the results regarding the global slope test.
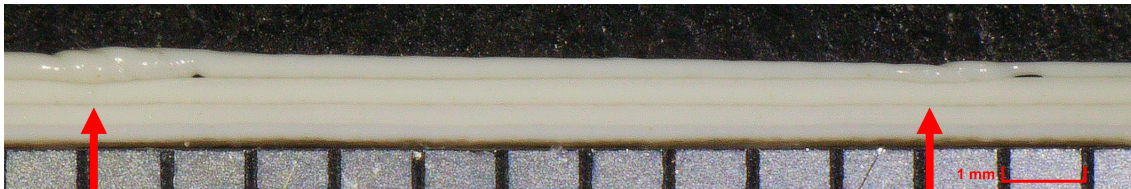
(a) Distance 10 mm, angle of $1.4°$ w.r.t. z-axis.

(b) Distance 5 mm, angle of $2.9°$ w.r.t. z-axis.

(c) Distance 4 mm, angle of $3.6°$ w.r.t. z-axis.
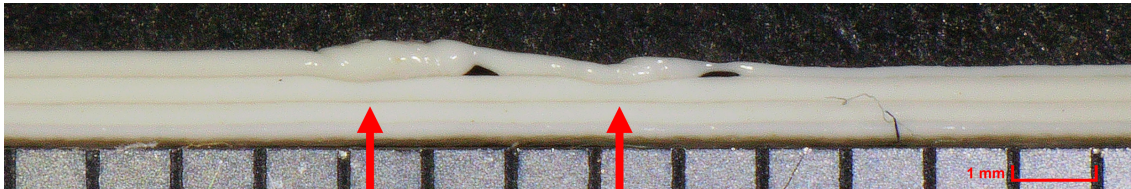
(d) Distance 3 mm, angle of $4.8°$ w.r.t. z-axis.
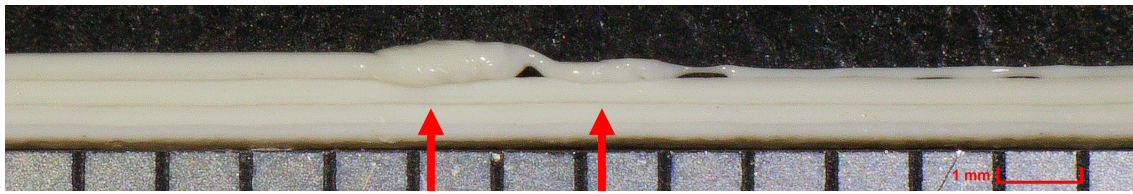
(e) Distance 2 mm, angle of 7.1° w.r.t. z-axis.
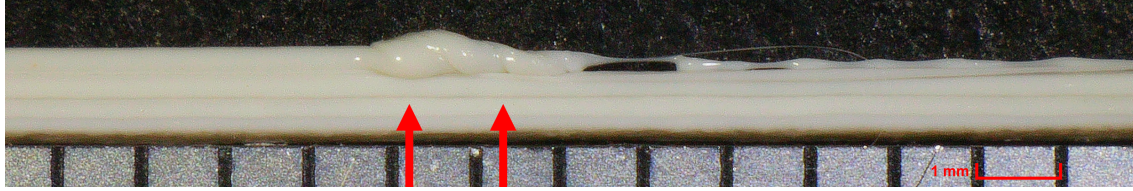
(f) Distance 1 mm, angle of 14.0° w.r.t. z-axis.

Figure B.1: Micrographs of the local slope test with rotation. The red arrow indicates the start and end point of the introduced slope.
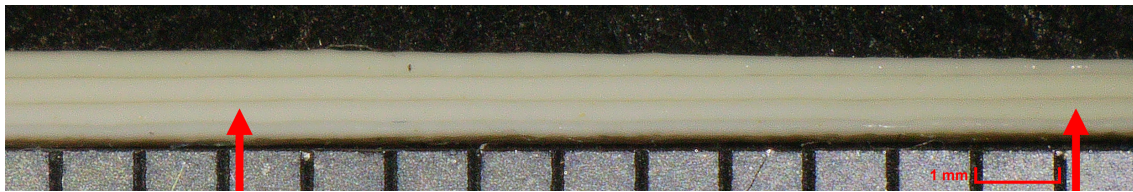
(a) Distance 10 mm, angle of 1.4° w.r.t. z-axis.
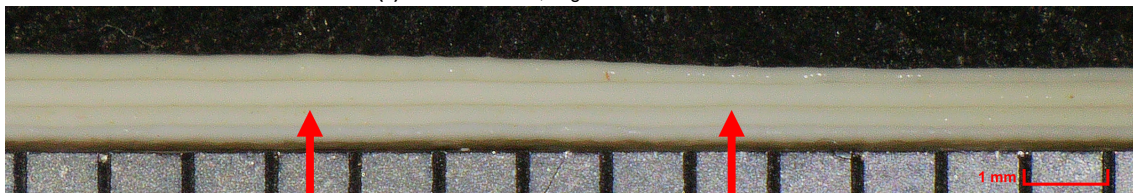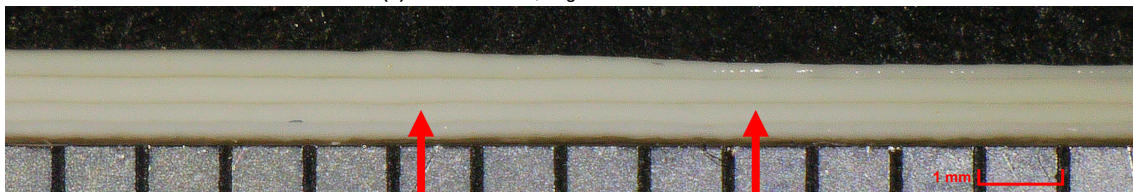
(b) Distance 5 mm, angle of 2.9° w.r.t. z-axis.

(c) Distance 4 mm, angle of 3.6° w.r.t. z-axis.
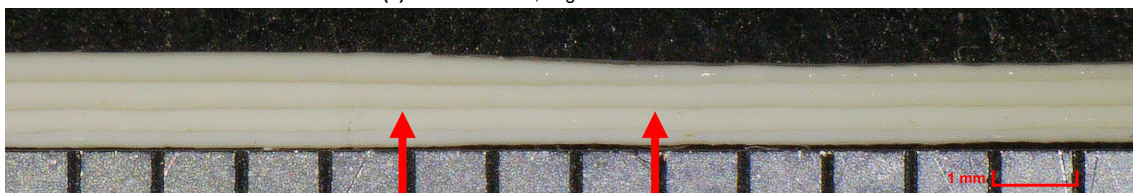
(d) Distance 3 mm, angle of 4.8° w.r.t. z-axis.
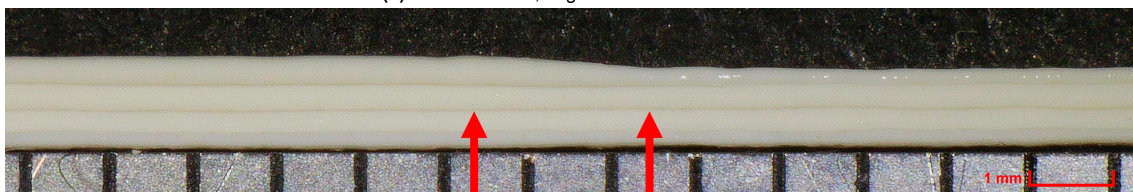
(e) Distance 2 mm, angle of 7.1° w.r.t. z-axis.
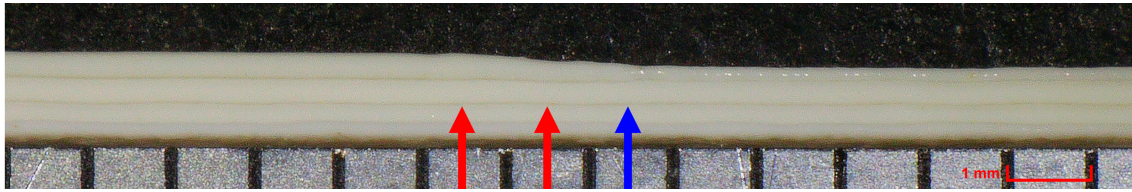
(f) Distance 1 mm, angle of 14.0° w.r.t. z-axis.
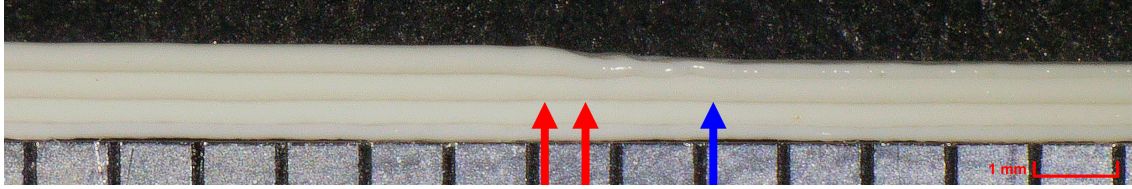
(g) Distance 0.5 mm, angle of 26.6° w.r.t. z-axis.

Figure B.2: Micrographs of the local slope test without rotation. The red arrow indicates the start and end point of the introduced slope. The blue arrow, if present, indicates the observed end point of the introduced slope.
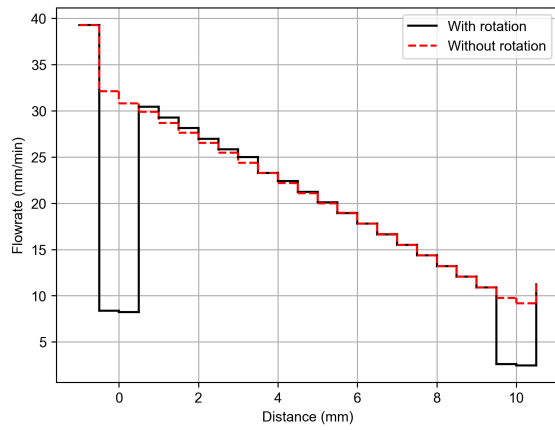
(a) Flow rate at each increment for a slope of 1.4° over 10 mm.
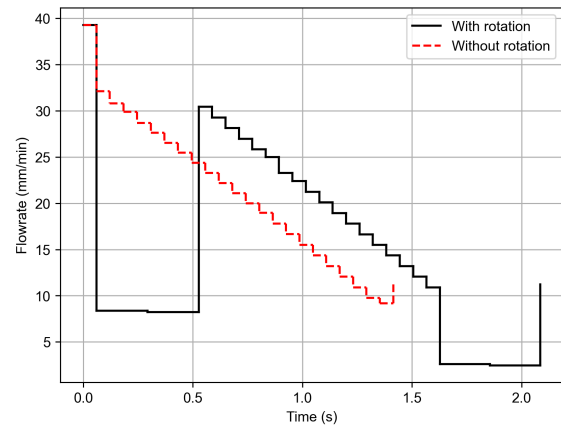
(b) Duration of each flow rate for a slope of 1.4° over 10 mm.
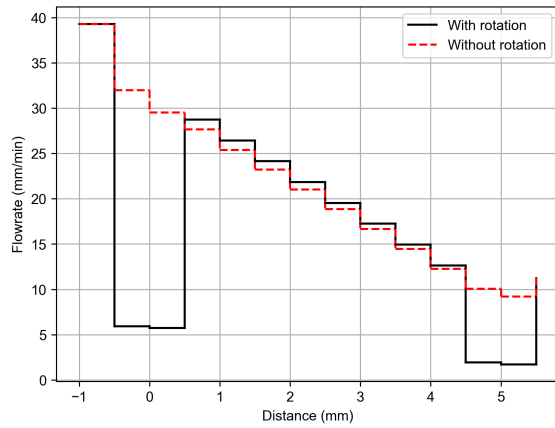
(c) Flow rate at each increment for a slope of 2.9° over 5 mm.
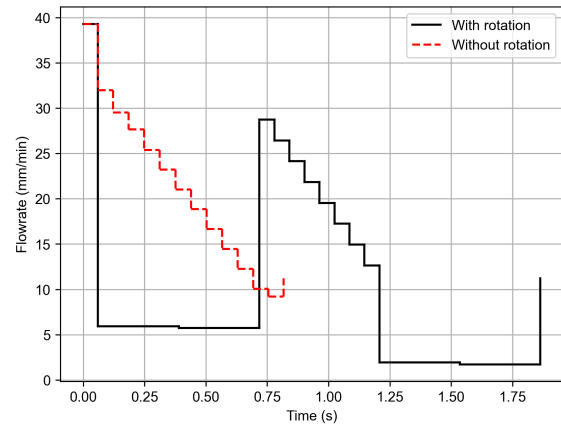
(d) Duration of each flow rate for a slope of 2.9° over 5 mm.
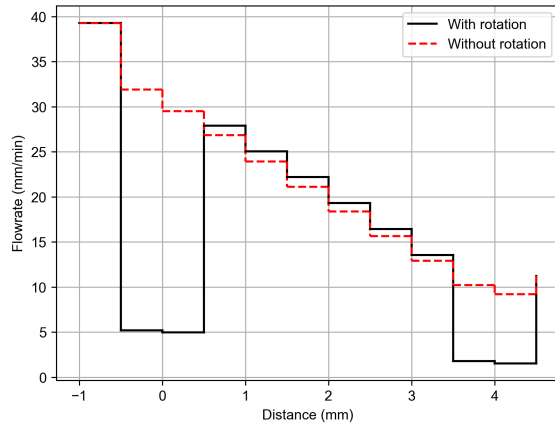
(e) Flow rate at each increment for a slope of 3.6° over 4 mm.
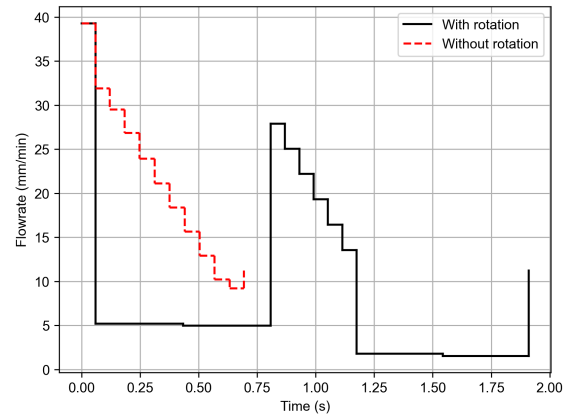
(f) Duration of each flow rate for a slope of 3.6° over 4 mm.
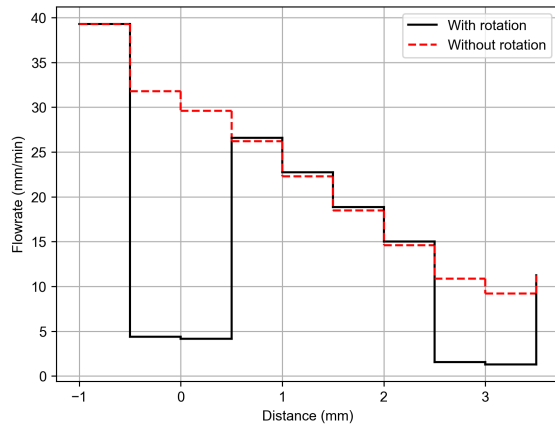
(g) Flow rate at each increment for a slope of 4.8° over 3 mm.
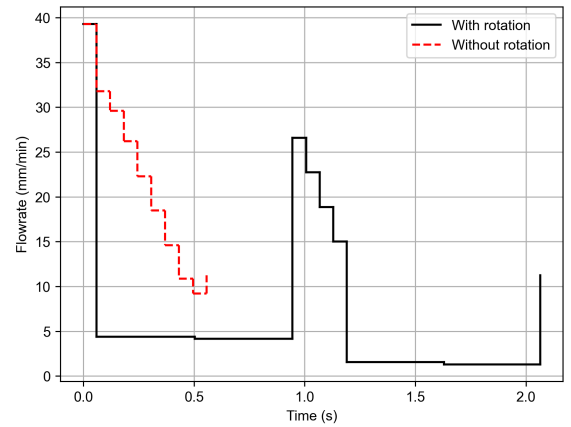
(h) Duration of each flow rate for a slope of 4.8° over 3 mm.
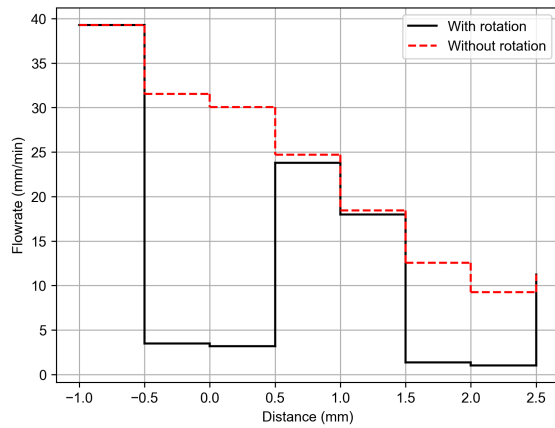
(i) Flow rate at each increment for a slope of 7.1° over 2 mm.
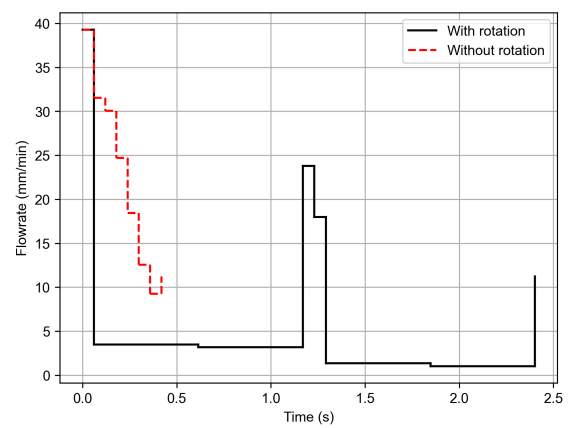
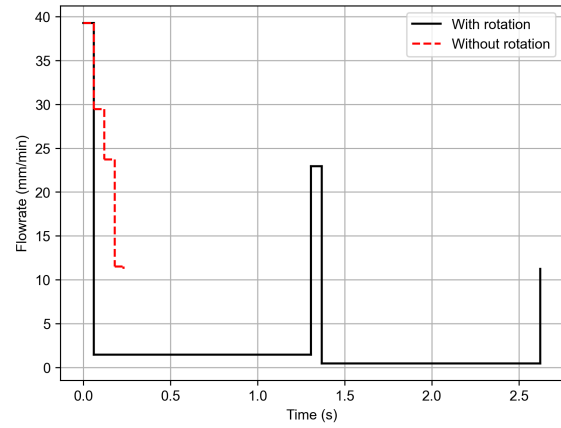**(j)** Duration of each flow rate for a slope of 7.1° over 2 mm.
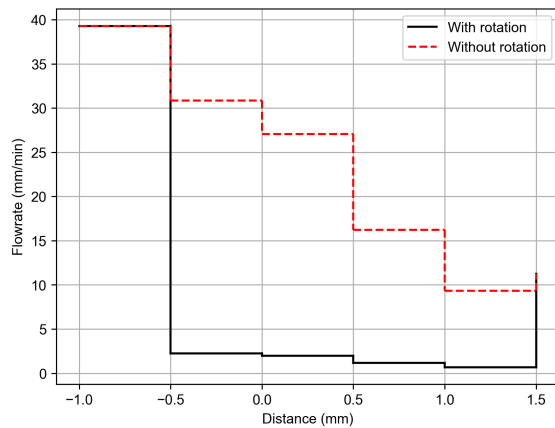
(k) Flow rate at each increment for a slope of 14.0° over 1 mm.
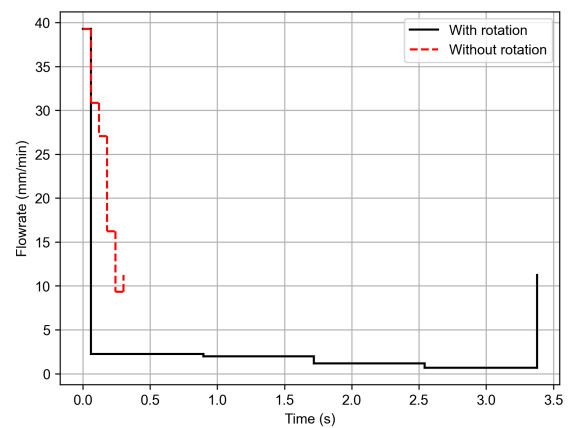
(l) Duration of each flow rate for a slope of 14.0° over 1 mm.
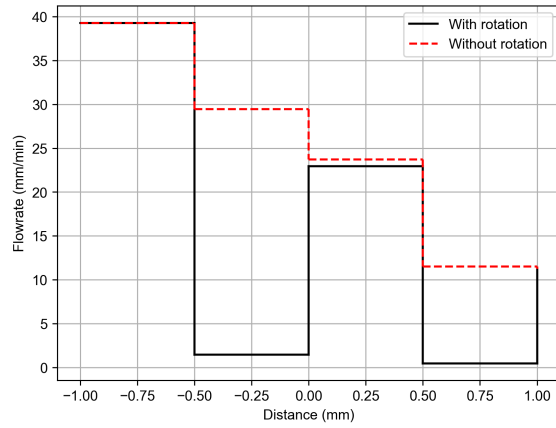
(m) Flow rate at each increment for a slope of 26.6° over 0.5 mm.
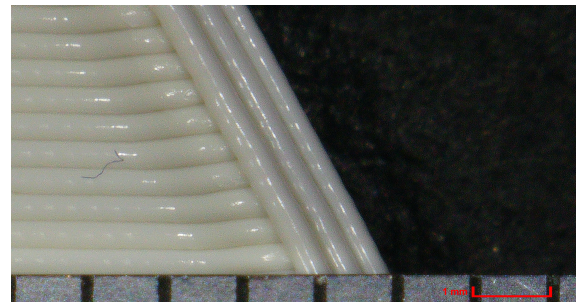
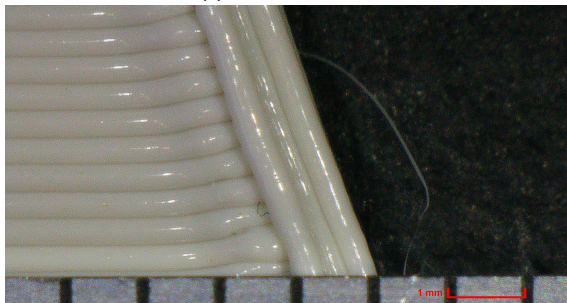**(n)** Duration of each flow rate for a slope of 26.6° over 0.5 mm.

Figure B.3: Several figures showing the relation between flow rate, time and location of the several tests.
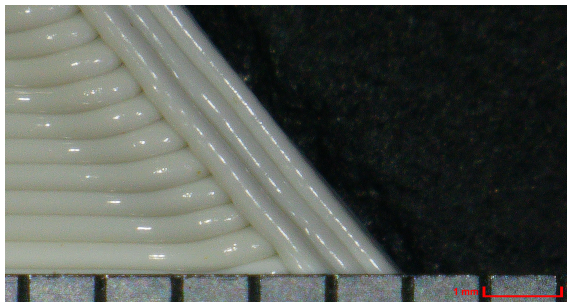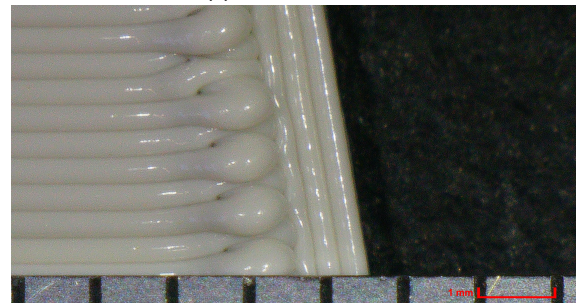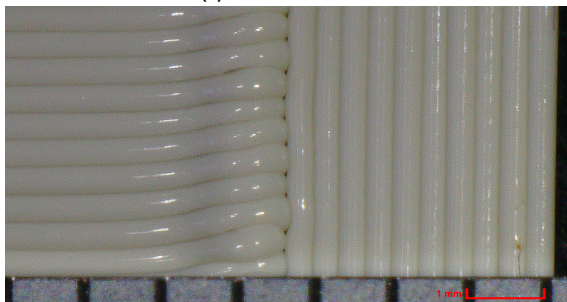

(a) Inclination of 50°.

(b) Inclination of 60°.

(c) Inclination of 70°.

(d) Inclination of 80°.

(e) Inclination of 90°.

(f) Clean inclination of 50°.

Figure B.4: Micrographs of the deposited layers on an inclined surfaces.